

Contents lists available at [ScienceDirect](https://www.sciencedirect.com)

Journal of Sound and Vibration

journal homepage: www.elsevier.com/locate/jsvi

High-order accurate transient and free-vibration analysis of plates and shells

Vincenzo Gulizzi ^{a,*}, Ivano Benedetti ^{a,b}, Alberto Milazzo ^{a,b}

^a Department of Engineering, University of Palermo, Viale delle Scienze, Building 8, Palermo, 90128, Italy

^b National Sustainable Mobility Center - Centro Nazionale per la Mobilità Sostenibile — CNMS, Italy

ARTICLE INFO

Keywords:

High-order accuracy
Discontinuous Galerkin methods
Composite shells
Transient analysis
Free-vibration analysis

ABSTRACT

The limited availability of analytical solutions and the high cost associated with experimental testing motivate the use of computational tools to assess the dynamic behavior of load-bearing components, especially when a wide design space must be explored, as is often the case with composite structures. In this context, a novel high-order accurate discontinuous Galerkin formulation for transient and free-vibration analysis of multilayered plates and shells is presented and numerically validated. The starting point of the formulation is a generalized structural theory for multilayered shells with arbitrary curvature based on the expansion of the displacement covariant components throughout the shell thickness. The variational statement of three-dimensional elastodynamics allows deriving the strong form of the governing differential equations, which form the basis to obtain the corresponding discontinuous Galerkin weak statements. As the order of the through-the-thickness expansion and the order of the discontinuous Galerkin basis functions are free parameters, the proposed approach allows tuning the order of accuracy of the computed solution throughout both the shell thickness and the shell modeling domain. Numerical results are reported and discussed for several validation test cases in terms of h - and p -convergence analyses, demonstrating the high-order accuracy, robustness, and computational savings of the formulation.

1. Introduction

Laminated composite plates and shells are today widely employed in several engineering applications, especially where it is important to achieve high structural stiffness at low weight, as in the automotive and aerospace sectors [1–4].

Recent advancements in manufacturing methods allow the fabrication of structural members or components whose shape, lay-up, and load paths may be tailored on their specific employment, thus granting the designers and engineers remarkable design freedom [5,6]. However, the accessibility of a larger design space requires the capability of the designer of objectively assessing a larger number of options for the intended application to select the most suitable structural configuration and/or architecture for considered function.

While experimental characterization and testing play an important role in the development of novel engineering products, especially at higher technology readiness levels, *virtual testing* has become a fundamental part of the earlier development process, when several alternative solutions need to be assessed, as typically happens in the conceptual design stage [7–11]. Indeed, the employment of fast, effective, and reliable computational models complements today the implementation of experimental campaigns,

* Corresponding author.

E-mail address: vincenzo.gulizzi@unipa.it (V. Gulizzi).

<https://doi.org/10.1016/j.jsv.2024.118479>

Received 23 February 2024; Accepted 27 April 2024

Available online 7 May 2024

0022-460X/© 2024 The Authors. Published by Elsevier Ltd. This is an open access article under the CC BY license (<http://creativecommons.org/licenses/by/4.0/>).

reducing their costs in terms of both time and hardware, and their availability constitutes an invaluable asset for engineers and manufacturers [12–14].

Depending on the specific application, the set of conditions for which functional and safe operation must be demonstrated varies from simple, well-defined static tests, to complex dynamic scenarios under multiple loads, up to impact tests that may involve the destruction of the component. In aircraft design, for example, where structural requirements are obviously very stringent, according to Title 14 CFR §25.305 – *Strength and deformation* – at letter (a) it is stipulated that *the structure must be able to support limit loads without detrimental permanent deformation. At any load up to limit loads, the deformation may not interfere with safe operation.* Moreover, at letter (e), it is required that *the airplane must be designed to withstand any vibration and buffeting that might occur in any likely operating condition [...]*, and, at letter (f), that *unless shown to be extremely improbable, the airplane must be designed to withstand any forced structural vibration resulting from any failure, malfunction or adverse condition in the flight control system [...]* and, in general, *this must be shown by analysis, flight tests, or other tests found necessary by the Administrator.* It is then apparent that both static and dynamic assessments are relevant.

In this context, the present contribution proposes a novel discontinuous Galerkin (DG) formulation for the linear free-vibration and transient analysis of isotropic and laminated plates and shells. Such structures feature inherent heterogeneity, which strongly affect their mechanical response, rendering their study a complex engineering task — further complicated by the presence of curvature in shells. While fully three-dimensional models are always an option, high-order structural theories built considering the characteristic component features, for example the small thickness of the plate or shell, are able to provide high accuracy at reduced computational costs. Plates and shells may be modeled using *Equivalent Single Layer* (ESL) theories, where the displacement components are assumed to vary according to assumed high-order functions throughout the thickness [15]. The plate or shell is thus replaced by an individual layer with equivalent mechanical properties and it is governed by a system of differential equations depending, in general, on two curvilinear variables. Such governing equations are generally solved employing approximate numerical schemes, as analytical solutions are only available for a limited set of problems that do not cover the whole set of possible applications. The most widely employed numerical method for structural analysis is the Finite Element Method (FEM), whose application to the solution of dynamic problems of plates and shells modeled by variable-order structural theories is still an active topic of research, see, e.g., Refs. [16–19]. Other techniques have also been proposed in the literature with the aim to improve the flexibility of numerical schemes with respect to FEM. Examples include the meshless methods, which do not require a partition of the domain of analysis into elements and have been employed in conjunction with the First-order Shear Deformation Theory (FSDT) [20,21] as well as higher-order structural theories [22], or the Ritz methods, which offer a variational setting where boundary/interface conditions can be enforced either strongly by suitably modifying the set of basis functions [23–26] or weakly by suitable penalization techniques [27,28].

DG methods have also shown to be a powerful and flexible alternative, offering adjustable high-order accuracy over conventional and non-conventional meshes, and have been successfully employed for the static analysis of plates and shells, also in presence of complex morphological features and boundary conditions, as in the case of presence of cut-outs [29–31]. DG methods have also been used for eigenvalue problems (not related to shells), see, e.g., [32,33], and, more recently, for the linear buckling analysis of plates and shells [34]. However, a thorough investigation of the performance of DG methods for free-vibration and transient analysis of multilayered plates and shells appears lacking in the literature. It is therefore presented for the first time in this work. The considered shells, which include plate geometries as a particular case, are assumed to have a general curvature and are modeled using ESL kinematics in the displacement covariant components. The DG technique is then used to discretize the resulting governing equations in space, whereas the temporal integration is performed using a standard Newmark scheme.

The paper is organized as follows. Section 2 recalls the key items of the shell structural theory, namely its geometric description, the generalized kinematic assumption, the constitutive modeling, and retrieves the strong form of the shell dynamics equations starting from the appropriate variational statements. The strong form of the governing equations is the starting point for the development of the proposed DG formulation, whose derivation is presented in Section 3, where also different meshing strategies are described, including the employment of implicitly-defined meshes. Several test cases are then considered in Section 4, where different meshing schemes are employed and in-depth hp -convergence assessments for both isotropic and laminated plates and shells are performed, proving the accuracy and robustness of the method. Some possible avenues of future developments and the conclusions are eventually drawn.

2. Problem statement

In this section all the items entering the formulation of the structural shell theory are recalled. The geometry description is discussed in Section 2.1, the kinematic modeling in Section 2.2, and the constitutive description in Section 2.3. Eventually, the strong form of the shell dynamics equations, which provide the starting point for the subsequent DG formulation, is retrieved in Section 2.4 for transient and free-vibrations analysis.

2.1. Geometry description

The formulation is developed for shells whose geometry can be described as schematically illustrated in Fig. 1 and discussed in Refs. [31,34,35]. The shell can be analyzed identifying a *reference surface*, featuring general curvature, in the physical space $Ox_1x_2x_3$, and adopting over such surface a suitable parametrization based on the set of curvilinear coordinates (ξ_1, ξ_2) . The shell volume V in the coordinates system $Ox_1x_2x_3$ can thus be represented, and conveniently built, through a mapping $x : V_\xi \rightarrow V$ that

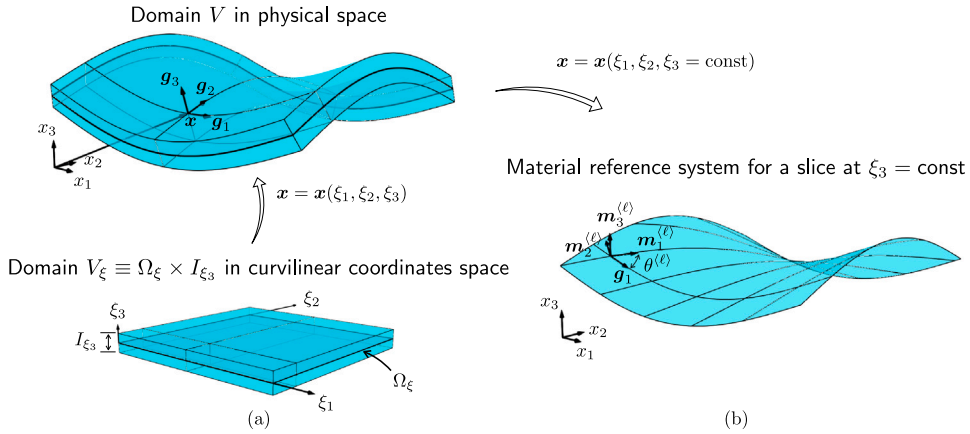


Fig. 1. (a) The geometry of the shell in the physical space $Ox_1x_2x_3$ can be described through the mapping $\mathbf{x} = \mathbf{x}(\xi_1, \xi_2, \xi_3)$, $\forall (\xi_1, \xi_2, \xi_3) \in V_\xi \equiv \Omega_\xi \times I_{\xi_3}$; once the mapping $\mathbf{x} = \mathbf{x}(\xi)$ is defined, the covariant basis vectors \mathbf{g}_k can be associated with it; (b) A material orthonormal basis \mathbf{m}_j can be defined to facilitate the description of the constitutive behavior of the different material layers, see Section 2.3.

associates the point $\mathbf{x} \in V$ to the natural coordinates $\xi = (\xi_1, \xi_2, \xi_3) \in V_\xi \equiv \Omega_\xi \times I_{\xi_3}$, as shown in Fig. 1(a), where Ω_ξ denotes the reference surface of the shell spanned by (ξ_1, ξ_2) in the curvilinear coordinates space and $I_{\xi_3} \equiv [-\zeta/2, \zeta/2]$ is the thickness interval spanned by ξ_3 . Under the above assumptions, the mapping can be expressed in the form

$$\mathbf{x} = \mathbf{x}(\xi_1, \xi_2, \xi_3) = \mathbf{x}_0(\xi_1, \xi_2) + \xi_3 \mathbf{n}_0(\xi_1, \xi_2) \quad \forall \xi \in V_\xi \quad (1)$$

where \mathbf{x}_0 is a generic point of the shell reference surface and \mathbf{n}_0 is the corresponding unit vector normal, which can be expressed as

$$\mathbf{n}_0 = \frac{\mathbf{a}_1 \times \mathbf{a}_2}{\|\mathbf{a}_1 \times \mathbf{a}_2\|} \quad \text{with} \quad \mathbf{a}_\alpha \equiv \frac{\partial \mathbf{x}_0}{\partial x_\alpha}. \quad (2)$$

Once the mapping in Eq. (1) has been introduced, it is possible to define, see Fig. 1(a), the covariant basis vectors as

$$\mathbf{g}_k \equiv \frac{\partial \mathbf{x}}{\partial \xi_k}, \quad k = 1, 2, 3 \quad (3)$$

that will be used to express the kinematic model in Section 2.2.

2.2. Shell kinematic model

The shell formulation is built starting from the kinematic ESL representation [15], which, following the matrix notation introduced in Ref. [30,35], is expressed as

$$\mathbf{u}_\xi = \mathbf{Z}(\xi_3) \mathbf{U}(\xi_1, \xi_2), \quad (4)$$

where \mathbf{u}_ξ collects the covariant components of the displacement field with respect to the contravariant basis \mathbf{g}^k , $k = 1, 2, 3$, defined as $\mathbf{g}^k \cdot \mathbf{g}_l = \delta_l^k$, while \mathbf{Z} is a $3 \times N_u$ matrix collecting the known thickness functions and \mathbf{U} is a N_u -dimensional vector collecting the unknown generalized displacement components. More specifically, $N_u = 3 + N_{u_1} + N_{u_2} + N_{u_3}$, where N_{u_i} expresses the order of expansion of the i -th displacement component. It worth noting that N_u and the expressions of the thickness functions contained in \mathbf{Z} depend on the selected structural ESL theory [29,30,35]. Following a consolidated notation [15], the theories generated by the kinematic model in Eq. (4) will be denoted in the remainder of the article as ED_{ijk} , with $i = N_{u_1}$, $j = N_{u_2}$, $k = N_{u_3}$. Note that the present formulation allows considering the FSDT as an ED_{110} theory where the plane stress hypothesis and the presence of shear factors are introduced in the constitutive behavior.

The displacement components can be expressed in the global Cartesian coordinate system $Ox_1x_2x_3$ – which simplifies the expression of the weak statement – through the transformation

$$\mathbf{u} = \mathbf{R}_\xi \mathbf{u}_\xi = \mathbf{R}_\xi \mathbf{Z}(\xi_3) \mathbf{U}(\xi_1, \xi_2), \quad (5)$$

where the k th column of the matrix \mathbf{R}_ξ collects the Cartesian components of \mathbf{g}^k . Subsequently, the derivatives with respect to the Cartesian coordinates can be retrieved applying the chain derivation rule, which leads to

$$\frac{\partial \mathbf{u}}{\partial x_k} = \mathbf{D}_{0k} \mathbf{U} + \mathbf{D}_{ak} \frac{\partial \mathbf{U}}{\partial \xi_a}, \quad (6)$$

where

$$\mathbf{D}_{0k} \equiv \frac{\partial \xi_j}{\partial x_k} \frac{\partial \mathbf{R}_\xi}{\partial \xi_j} \mathbf{Z} + \frac{\partial \xi_3}{\partial x_k} \mathbf{R}_\xi \frac{d\mathbf{Z}}{d\xi_3} \quad \text{and} \quad \mathbf{D}_{ak} \equiv \frac{\partial \xi_a}{\partial x_k} \mathbf{R}_\xi \mathbf{Z}, \quad (7)$$

and implicit summation with respect to the repeated indexes is assumed, according to the Einstein notation, with the caveat that Greek indexes span the set $\{1, 2\}$, while Latin indexes span the set $\{1, 2, 3\}$ throughout the paper.

The Cartesian components of the small strain tensor, collected according to the Voigt notation, are retrieved from the kinematic model in Eq. (5) through the relationships

$$\boldsymbol{\gamma} = \mathbf{I}_k \frac{\partial \mathbf{u}}{\partial x_k} = \mathbf{J}_0 \mathbf{U} + \mathbf{J}_\alpha \frac{\partial \mathbf{U}}{\partial \xi_\alpha}, \quad (8)$$

where \mathbf{I}_k are matrices whose entries are either 0 or 1, see e.g. Ref. [29], and

$$\mathbf{J}_0 \equiv \mathbf{I}_k \mathbf{D}_{0k} \quad \text{and} \quad \mathbf{J}_\alpha \equiv \mathbf{I}_k \mathbf{D}_{\alpha k} \quad (9)$$

with $\alpha = 1, 2$ and $k = 1, 2, 3$.

2.3. Constitutive behavior

In composite laminated shells, the point \mathbf{x} spans different material layers as ξ_3 varies. If ξ_3 is kept constant and only (ξ_1, ξ_2) are varied, \mathbf{x} spans a surface embedded in a certain material layer, for which some specific material reference directions can be identified, as for example in the case of fiber reinforced composites, where a material reference system is identified by the fibers direction and their transverse plane. At each point (ξ_1, ξ_2, ξ_3) of a material layer, an angle θ between the relevant material direction and the covariant vector \mathbf{g}_1 can be identified. A local *material* Cartesian reference basis $\mathbf{m}_k^{(\ell)}$ can then be attached to each point of the generic composite layer $\langle \ell \rangle$ through the relationships

$$\mathbf{m}_1^{(\ell)} \equiv \mathbf{R}_{n_0}(\theta^{(\ell)}) \frac{\mathbf{g}_1}{\|\mathbf{g}_1\|}, \quad \mathbf{m}_3^{(\ell)} \equiv \mathbf{n}_0, \quad \text{and} \quad \mathbf{m}_2^{(\ell)} \equiv \mathbf{m}_3^{(\ell)} \times \mathbf{m}_1^{(\ell)}. \quad (10)$$

In the material reference basis $\mathbf{m}_k^{(\ell)}$, the constitutive law is expressed in Voigt notation as

$$\tilde{\boldsymbol{\sigma}}^{(\ell)} = \tilde{\mathbf{C}}^{(\ell)} \tilde{\boldsymbol{\gamma}}^{(\ell)} \quad (11)$$

where the form of the matrix $\tilde{\mathbf{C}}$ directly reflects the existing material symmetries (e.g. isotropy, orthotropy, etc.). The stress–strain relationship linking the components of the stress and strain tensors in the global reference system $Ox_1x_2x_3$ can thus be obtained from Eq. (11) through the standard transformation rules [36,37], leading to

$$\boldsymbol{\sigma}^{(\ell)} = \mathbf{C}^{(\ell)} \boldsymbol{\gamma}, \quad (12)$$

which simplifies the expression of the variational statement in the next sections.

2.4. Governing equations for shell dynamic analysis

The variational statement providing the weak formulation of the shell dynamic problem can be written resorting to the d'Alembert principle and treating the inertial term as a volume force term in the classical expression of the *principle of virtual displacements*, which, in the global Cartesian reference system $Ox_1x_2x_3$, leads to

$$\sum_{\ell=1}^{N_\ell} \int_{V^{(\ell)}} \delta \mathbf{u}^T \rho^{(\ell)} \frac{\partial^2 \mathbf{u}}{\partial t^2} dV + \sum_{\ell=1}^{N_\ell} \int_{V^{(\ell)}} \delta \boldsymbol{\gamma}^T \boldsymbol{\sigma}^{(\ell)} dV = \sum_{\ell=1}^{N_\ell} \int_{V^{(\ell)}} \delta \mathbf{u}^T \bar{\mathbf{b}} dV + \sum_{\ell=1}^{N_\ell} \int_{\partial V^{(\ell)}} \delta \mathbf{u}^T \bar{\mathbf{t}} dS, \quad (13)$$

where $\delta \cdot$ denotes the first variation operator, $\rho^{(\ell)}$ is the mass density of the layer ℓ , $\bar{\mathbf{b}}$ is the known volume force term, $\bar{\mathbf{t}}$ is the known surface traction and the summation is extended over the N_ℓ layers of the laminated shell. Employing the kinematic model in Eq. (5), the strain–displacement relationships in Eq. (8) and the constitutive relations in Eq. (12) and expanding the first variation, the above variational statement leads to

$$\begin{aligned} & \int_{\Omega_\xi} \delta \mathbf{U}^T \mathbf{M} \frac{\partial^2 \mathbf{U}}{\partial t^2} d\Omega_\xi + \int_{\Omega_\xi} \left[\frac{\partial \delta \mathbf{U}^T}{\partial \xi_\alpha} \left(\mathbf{Q}_{\alpha\beta} \frac{\partial \mathbf{U}}{\partial \xi_\beta} + \mathbf{R}_\alpha \mathbf{U} \right) + \delta \mathbf{U}^T \left(\mathbf{R}_\alpha^T \frac{\partial \mathbf{U}}{\partial \xi_\alpha} + \mathbf{S} \mathbf{U} \right) \right] d\Omega_\xi = \\ & = \int_{\Omega_\xi} \delta \mathbf{U}^T \bar{\mathbf{B}} d\Omega_\xi + \int_{\partial \Omega_\xi} \delta \mathbf{U}^T \bar{\mathbf{T}} d\partial \Omega_\xi, \end{aligned} \quad (14)$$

where

$$\mathbf{M} \equiv \sum_{\ell=1}^{N_\ell} \int_{\xi_{3b}^{(\ell)}}^{\xi_{3t}^{(\ell)}} \mathbf{Z}^T \mathbf{R}_\xi^T \rho^{(\ell)} \mathbf{R}_\xi \mathbf{Z} \sqrt{g} d\xi_3 \quad (15)$$

is a generalized mass matrix, the terms

$$\mathbf{Q}_{\alpha\beta} \equiv \sum_{\ell=1}^{N_\ell} \int_{\xi_{3b}^{(\ell)}}^{\xi_{3t}^{(\ell)}} \mathbf{J}_\alpha^T \mathbf{C}^{(\ell)} \mathbf{J}_\beta \sqrt{g} d\xi_3, \quad (16a)$$

$$\mathbf{R}_\alpha \equiv \sum_{\ell=1}^{N_\ell} \int_{\xi_{3b}^{(\ell)}}^{\xi_{3t}^{(\ell)}} \mathbf{J}_\alpha^T \mathbf{C}^{(\ell)} \mathbf{J}_0 \sqrt{g} d\xi_3 \quad (16b)$$

and

$$S \equiv \sum_{\ell=1}^{N_\ell} \int_{\xi_3^b}^{\xi_3^t} J_0^{\ell} C^{(\ell)} J_0 \sqrt{g} d\xi_3, \tag{16c}$$

are generalized stiffness matrices, whereas the terms

$$\bar{B} \equiv \left(Z^T R_\xi^T \bar{t} \sqrt{g} \sqrt{n_i g^{ij} n_j} \right)_{\xi_3=\pm\zeta/2} + \int_{-\zeta/2}^{\zeta/2} Z^T R_\xi^T \bar{b} \sqrt{g} d\xi_3 \tag{17a}$$

and

$$\bar{T} \equiv \int_{-\zeta/2}^{\zeta/2} Z^T R_\xi^T \bar{t} \sqrt{g} \sqrt{n_i g^{ij} n_j} d\xi_3 \tag{17b}$$

are generalized volume forces and generalized boundary tractions respectively. In Eqs. (15) to (17), g is the determinant of the metric tensor and $g^{ij} \equiv g^i \cdot g^j$ are its contravariant components. Additionally, in Eq. (17), the first term represents the surface traction applied over the top and bottom surfaces of the shell, while n_i is the i th component of the unit vector normal to the shell surface.

The variational statement in Eq. (14) is used to derive the strong form of the equations for the shell dynamics, which provides the starting point for the development of the DG formulation discussed in Section 3. In particular, performing the integration by parts and applying the standard rules of the calculus of variations, Eq. (14) leads to the following set of generalized equilibrium equations

$$M \frac{\partial^2 U}{\partial t^2} - \frac{\partial}{\partial \xi_\alpha} \left(Q_{\alpha\beta} \frac{\partial U}{\partial \xi_\beta} + R_\alpha U \right) + R_\alpha^T \frac{\partial U}{\partial \xi_\alpha} + S U = \bar{B}, \quad \text{in } [0, T] \times \Omega_\xi, \tag{18}$$

with the associated essential and natural generalized boundary conditions (GBCs) and the generalized initial conditions (GICs) defined as

$$\text{GBCs : } \begin{cases} U = \bar{U} & \text{in } [0, T] \times \partial\Omega_\xi^D \\ v_\alpha \left(Q_{\alpha\beta} \frac{\partial U}{\partial \xi_\beta} + R_\alpha U \right) = \bar{T} & \text{in } [0, T] \times \partial\Omega_\xi^N \end{cases} \tag{19a}$$

and

$$\text{GICs : } \begin{cases} U|_{t=0} = U_0 \\ \frac{\partial U}{\partial t}|_{t=0} = \dot{U}_0 \end{cases} \quad \text{in } \Omega_\xi, \tag{19b}$$

where T defines the width of the analyzed time window, $\partial\Omega_\xi^D$ and $\partial\Omega_\xi^N$ are the regions of the boundary $\partial\Omega_\xi$ of the analysis domain Ω_ξ over which Dirichlet (essential) or Neumann (natural) boundary conditions are assigned, respectively, v_α is the α th component of the unit vector normal to $\partial\Omega_\xi$; over-bars denote known boundary conditions on either generalized displacements or tractions, which may also depend on time, and the subscript 0 denotes known initial conditions.

Eventually, free vibrations are investigated by neglecting the external loads and assuming, as customary, harmonic response with unknown frequency ω and homogeneous kinematic boundary conditions, leading to the following eigenvalue problem

$$- \frac{\partial}{\partial \xi_\alpha} \left(Q_{\alpha\beta} \frac{\partial U}{\partial \xi_\beta} + R_\alpha U \right) + R_\alpha^T \frac{\partial U}{\partial \xi_\alpha} + (S - \omega^2 M) U = 0, \quad \text{in } \Omega_\xi. \tag{20}$$

3. Discontinuous Galerkin formulation

In this section, the recently-developed DG formulation for the mechanical behavior of structural components, such as beams [38], plates [29,30,39] and shells [31,34,35], is extended to solve the partial differential equations introduced in the preceding section for either transient analysis, see Eqs. (18) and (19), or free-vibration analysis, see Eq. (20), of composite shells.

Similar to other domain-based numerical techniques, such as the FEM, a DG-based approach requires a suitable partition of the domain where the governing equations are defined. Here, such a domain is Ω_ξ , which is partitioned into N_e non-overlapping elements, i.e., $\Omega_\xi \approx \Omega_\xi^h \equiv \bigcup_{e=1}^{N_e} \Omega_\xi^e$, where Ω_ξ^e is a generic e th element. The mesh leads to a partition of the boundary $\partial\Omega_\xi^D \approx \partial\Omega_\xi^{Dh} \equiv \bigcup_{e=1}^{N_e} \partial\Omega_\xi^{De}$ and the boundary $\partial\Omega_\xi^N \approx \partial\Omega_\xi^{Nh} \equiv \bigcup_{e=1}^{N_e} \partial\Omega_\xi^{Ne}$, where $\partial\Omega_\xi^{De}$ and $\partial\Omega_\xi^{Ne}$ are the portions the e th element's boundary where Dirichlet and Neumann boundary conditions, respectively, are enforced; is it clear that, for some elements, these boundaries can be empty sets. The mesh also leads to the set of inter-element interfaces $\partial\Omega_\xi^{Ih} \equiv \bigcup_{i=1}^{N_i} \partial\Omega_\xi^i$, where $\partial\Omega_\xi^i$ is the i th generic interface.

Then, the so-called broken integrals are defined as follows

$$\int_{\Omega_\xi^h} \bullet \equiv \sum_{e=1}^{N_e} \int_{\Omega_\xi^e} \bullet d\Omega_\xi, \tag{21a}$$

$$\int_{\partial\Omega_\xi^{Dh}} \bullet \equiv \sum_{e=1}^{N_e} \int_{\partial\Omega_\xi^{De}} \bullet d\partial\Omega_\xi, \quad \int_{\partial\Omega_\xi^{Nh}} \bullet \equiv \sum_{e=1}^{N_e} \int_{\partial\Omega_\xi^{Ne}} \bullet d\partial\Omega_\xi, \tag{21b}$$

and

$$\int_{\partial\Omega_\xi^h} \bullet \equiv \sum_{i=1}^{N_i} \int_{\partial\Omega_\xi^i} \bullet^i d\partial\Omega_\xi^i. \quad (21c)$$

Additionally, it is possible to define the average operator $\{\bullet\}^i$ and the jump operator $\llbracket \bullet \rrbracket_\alpha^i$ at the generic i th interface between the e th and e' th elements as

$$\{\bullet\}^i \equiv \frac{1}{2} (\bullet^e + \bullet^{e'}) \quad \text{and} \quad \llbracket \bullet \rrbracket_\alpha^i \equiv v_\alpha^e \bullet^e + v_\alpha^{e'} \bullet^{e'}, \quad (22)$$

where v_α^e is the α th component of the outer unit normal vector $\mathbf{v}^e \equiv (v_1^e, v_2^e)$ to the e th element's boundary.

Once the domain partition has been selected, the space of discontinuous basis functions is introduced as

$$\mathcal{V}_{hp} \equiv \{v : \Omega_\xi^h \rightarrow \mathbb{R} \mid v(\Omega_\xi^e) \in \mathcal{P}_p^e \forall e = 1, \dots, N_e\}, \quad (23)$$

where \mathcal{P}_p^e is the space of polynomials up to degree p defined over the element Ω_ξ^e . The corresponding space of discontinuous N_u -dimensional vector basis functions is then denoted by $\mathcal{V}_{hp}^{N_u} \equiv (\mathcal{V}_{hp})^{N_u}$. The DG formulations for transient and free-vibration analysis of composite shells are presented in the next two sections.

3.1. Transient analysis

Upon following the same steps discussed, e.g., in Refs. [31,34,35], it is possible to show that the weak DG formulation corresponding to Eqs. (18) and (19) reads: find $\mathbf{U}^h \in \mathcal{V}_{hp}^{N_u}$ such that

$$B_M(\mathbf{V}, \mathbf{U}^h) + B_K(\mathbf{V}, \mathbf{U}^h) = L(\mathbf{V}, \overline{\mathbf{B}}, \overline{\mathbf{T}}, \overline{\mathbf{U}}), \quad \forall \mathbf{V} \in \mathcal{V}_{hp}^{N_u}, \quad (24)$$

subjected to the approximate initial conditions

$$\begin{cases} \int_{\Omega_\xi^h} \mathbf{V}^\top \mathbf{U}^h = \int_{\Omega_\xi^h} \mathbf{V}^\top \mathbf{U}_0 \\ \int_{\Omega_\xi^h} \mathbf{V}^\top \frac{\partial \mathbf{U}^h}{\partial t} = \int_{\Omega_\xi^h} \mathbf{V}^\top \dot{\mathbf{U}}_0, \end{cases} \quad \forall \mathbf{V} \in \mathcal{V}_{hp}^{N_u}. \quad (25)$$

In Eqs. (24) and (25), \mathbf{U}^h denotes the approximate DG solution, the bilinear forms $B_M(\mathbf{V}, \mathbf{U}^h)$ and $B_K(\mathbf{V}, \mathbf{U}^h)$ are defined as

$$B_M(\mathbf{V}, \mathbf{U}^h) \equiv \int_{\Omega_\xi^h} \mathbf{V}^\top \mathbf{M} \frac{\partial^2 \mathbf{U}^h}{\partial t^2} \quad (26)$$

and

$$\begin{aligned} B_K(\mathbf{V}, \mathbf{U}^h) \equiv & \int_{\Omega_\xi^h} \frac{\partial \mathbf{V}^\top}{\partial \xi_\alpha} \left(\mathbf{Q}_{\alpha\beta} \frac{\partial \mathbf{U}^h}{\partial \xi_\beta} + \mathbf{R}_\alpha \mathbf{U}^h \right) + \mathbf{V}^\top \left(\mathbf{R}_\alpha^\top \frac{\partial \mathbf{U}^h}{\partial \xi_\alpha} + \mathbf{S} \mathbf{U}^h \right) + \\ & - \int_{\partial\Omega_\xi^h} \llbracket \mathbf{V} \rrbracket_\alpha^i \left\{ \mathbf{Q}_{\alpha\beta} \frac{\partial \mathbf{U}^h}{\partial \xi_\beta} + \mathbf{R}_\alpha \mathbf{U}^h \right\} + \left\{ \frac{\partial \mathbf{V}^\top}{\partial \xi_\alpha} \mathbf{Q}_{\alpha\beta} + \mathbf{V}^\top \mathbf{R}_\beta^\top \right\} \llbracket \mathbf{U}^h \rrbracket_\beta + \int_{\partial\Omega_\xi^h} \mu \llbracket \mathbf{V} \rrbracket_\alpha^i \llbracket \mathbf{U}^h \rrbracket_\alpha + \\ & - \int_{\partial\Omega_\xi^{Dh}} v_\alpha \mathbf{V}^\top \left(\mathbf{Q}_{\alpha\beta} \frac{\partial \mathbf{U}^h}{\partial \xi_\beta} + \mathbf{R}_\alpha \mathbf{U}^h \right) + \left(\frac{\partial \mathbf{V}^\top}{\partial \xi_\alpha} \mathbf{Q}_{\alpha\beta} + \mathbf{V}^\top \mathbf{R}_\beta^\top \right) \mathbf{U}^h v_\beta + \int_{\partial\Omega_\xi^{Dh}} \mu \mathbf{V}^\top \mathbf{U}^h, \end{aligned} \quad (27)$$

and the linear form $L(\mathbf{V}, \overline{\mathbf{B}}, \overline{\mathbf{T}}, \overline{\mathbf{U}})$ reads

$$L(\mathbf{V}, \overline{\mathbf{B}}, \overline{\mathbf{T}}, \overline{\mathbf{U}}) \equiv \int_{\Omega_\xi^h} \mathbf{V}^\top \overline{\mathbf{B}} + \int_{\partial\Omega_\xi^{Nh}} \mathbf{V}^\top \overline{\mathbf{T}} - \int_{\partial\Omega_\xi^{Dh}} \left(\frac{\partial \mathbf{V}^\top}{\partial \xi_\alpha} \mathbf{Q}_{\alpha\beta} + \mathbf{V}^\top \mathbf{R}_\beta^\top \right) \overline{\mathbf{U}} v_\beta + \int_{\partial\Omega_\xi^{Dh}} \mu \mathbf{V}^\top \overline{\mathbf{U}}. \quad (28)$$

3.2. Free-vibration analysis

In case of free-vibration analysis, it is possible to show the weak DG formulation corresponding to Eq. (20) reads: find $(\omega, \mathbf{U}^h) \in \mathbb{R} \times \mathcal{V}_{hp}^{N_u}$ such that

$$-B_\omega(\mathbf{V}, \mathbf{U}^h, \omega) + B_K(\mathbf{V}, \mathbf{U}^h) = 0 \quad \forall \mathbf{V} \in \mathcal{V}_{hp}^{N_u} \quad (29)$$

where

$$B_\omega(\mathbf{V}, \mathbf{U}^h, \omega) \equiv \omega^2 \int_{\Omega_\xi^h} \mathbf{V}^\top \mathbf{M} \mathbf{U}^h. \quad (30)$$

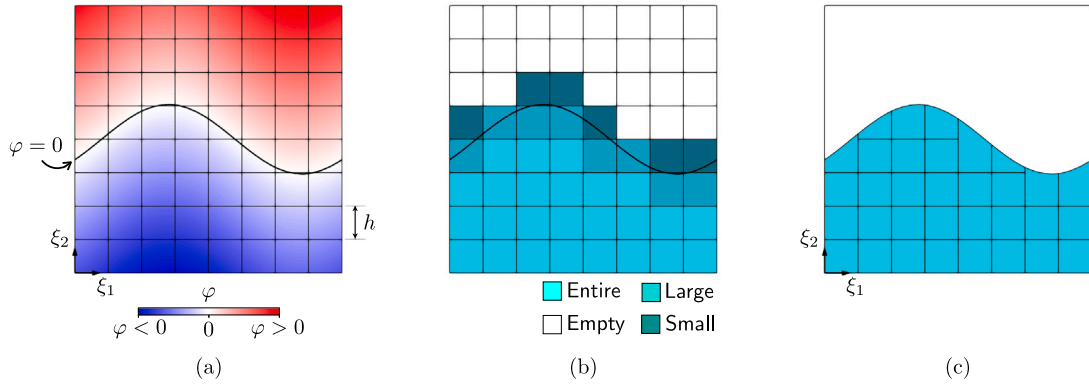


Fig. 2. (a) Level set function. (b) Cell classification based on the volume fraction. (c) Implicitly-defined mesh.

3.3. Meshing

The DG formulation presented in this section is not limited to a specific domain partition strategy. In fact, it could be employed in conjunction with both conventional partitions, such as structured or unstructured meshes, and less conventional ones, such as polygonal or implicitly-defined meshes.

In this work, we consider both structured meshes and implicitly-defined meshes, which are briefly described in this section. Let us assume that the curvilinear coordinates (ξ_1, ξ_2) span a rectangle $R_\xi \equiv [\xi_1^L, \xi_1^U] \times [\xi_2^L, \xi_2^U]$, where (ξ_1^L, ξ_2^L) and (ξ_1^U, ξ_2^U) are the bottom-left and top-right corners, respectively, of the rectangle. The rectangle is then partitioned using a structured grid of $n_1 \times n_2$ cells of size $h_1 \equiv (\xi_1^U - \xi_1^L)/n_1$ and $h_2 \equiv (\xi_2^U - \xi_2^L)/n_2$, such that a generic c th cell R_ξ^c may be identified by $R_\xi^c \equiv [\xi_1^L + \iota_1 h_1, \xi_1^L + (\iota_1 + 1)h_1] \times [\xi_2^L + \iota_2 h_2, \xi_2^L + (\iota_2 + 1)h_2]$, with $\iota_1 = 0, \dots, (n_1 - 1)$ and $\iota_2 = 0, \dots, (n_2 - 1)$.

In case of structured meshes, the domain Ω_ξ simply coincides with R_ξ , each element Ω_ξ^e coincides with one of the grid cell, and the total number of elements is $N_e = n_1 n_2$.

In case of implicitly-defined meshes, R_ξ represents a background space containing the domain Ω_ξ , which is implicitly-defined by a level set function $\varphi : R_\xi \rightarrow \mathbb{R}$ as follows

$$\Omega_\xi \equiv \{(\xi_1, \xi_2) \in R_\xi : \varphi(\xi_1, \xi_2) < 0\}. \tag{31}$$

Similarly, the boundary $\partial\Omega_\xi$ is defined as

$$\partial\Omega_\xi \equiv \{(\xi_1, \xi_2) \in \partial R_\xi : \varphi(\xi_1, \xi_2) < 0\} \cup \{(\xi_1, \xi_2) \in R_\xi : \varphi(\xi_1, \xi_2) = 0\}, \tag{32}$$

where ∂R_ξ is the boundary of R_ξ . Then, the partition of Ω_ξ is obtained by intersecting Ω_ξ with the structured grid defined for R_ξ . Such an intersection leads to a classification of the grid cells. In particular, one obtains: *entire* cells falling entirely within Ω_ξ , *empty* cells falling entirely outside Ω_ξ , and partial cells that are cut by the zero-contour of the level set function φ . Partial cells are further classified based on their volume fraction into *large* cells, which have a volume fraction above a certain user-defined threshold, and *small* cells, which are the remaining partial cells. Each small cell is then merged with the one neighboring cell that has the largest volume fraction. Such a merging procedure allows avoiding the presence of overly small elements, which would ill-condition the algebraic system of equations. Eventually, the mesh elements are defined as the set of entire, large and merged cells.

An illustration of the construction of the implicitly-defined mesh as discussed above is reported in Fig. 2, which shows a level set function φ defined over a square that is partitioned with an 8×8 grid of mesh size h , see Fig. 2(a), the corresponding cell classification, see Fig. 2(b), and the obtained implicitly-defined mesh after the cell-merging procedure, see Fig. 2(c).

Finally, it is worth noting that, the implicit definition of Ω_ξ as given in Eq. (31) allows introducing curved boundaries into the space of curvilinear coordinates, thereby extending the space of shell geometries that can be modeled within the present framework whilst retaining the simplicity of structured mesh generation. Additionally, the discontinuous nature of DG methods combined with the use of high-order accurate quadrature rules for implicitly-defined domains and boundaries allows obtaining a high-order accurate solution of the governing equations also in case of implicitly-defined geometries. The interested reader is referred to Refs. [40–43] for a more extensive discussion on the combined use of implicitly-defined meshes, including adaptive mesh refinement, and DG methods for two- and three-dimensional problems.

4. Results

The developed formulation has been implemented in PySCo,¹ a collection of python routines for scientific computing, and tested with several test cases, whose results are reported and discussed in the present section.

¹ <https://gitlab.com/aeropa/pysco>.

Table 1
Properties of the considered materials.

Material ID	Property	Component	Value
M ₁	Young's modulus	E	1
	Poisson's ratios	ν	0.25
	Density	ρ	1
M ₂	Young's moduli	E_1	25
		E_2, E_3	1
	Poisson's ratios	$\nu_{23}, \nu_{13}, \nu_{12}$	0.25
	Shear moduli	G_{23}	0.2
		G_{13}, G_{12}	0.5
	Density	ρ	1

Table 2
Properties of the considered plate/shell sections.

Shell ID	Material	Layup	Layer(s) thickness
P ₁	M ₁	[0]	ζ
P ₂	M ₂	[0/90] ₂	$\zeta/4$
C ₁	M ₁	[0]	ζ
C ₂	M ₂	[0/90] ₂	$\zeta/4$
S ₁	M ₁	[0]	ζ

Plates and shells with different material layups have been analyzed. Table 1 summarizes the mechanical properties of the materials M₁, isotropic, and M₂, transversely isotropic, used for the individual plies. Table 2 details the layups, labeled as P₁, P₂, C₁, C₂, S₁, considered for the analyzed plates and shells.

For all the considered cases, relevant hp -convergence analyses have been performed, considering both the characteristic size h of the mesh and the order p of the DG basis functions, which here consist of tensor-product Legendre polynomials. The obtained results have been presented upon introducing the following error measures:

$$e_\omega \equiv \frac{|\omega^h - \omega^{\text{ref}}|}{|\omega^{\text{ref}}|}, \quad e_U \equiv \frac{\|U^h - U^{\text{ref}}\|_{L_\infty(\Omega_\xi^h)}}{\|U^{\text{ref}}\|_{L_\infty(\Omega_\xi^h)}} \quad \text{and} \quad e_{\nabla U} \equiv \frac{\|U^h - U^{\text{ref}}\|_{W_\infty^1(\Omega_\xi^h)}}{\|U^{\text{ref}}\|_{W_\infty^1(\Omega_\xi^h)}} \quad (33)$$

where the superscript h refers to the scalar or vector output provided by the proposed DG-based numerical scheme, the superscript ref refers to the considered reference solution, while $\|\cdot\|_{L_\infty(\Omega_\xi^h)}$ and $\|\cdot\|_{W_\infty^1(\Omega_\xi^h)}$ are the standard L_∞ norm and W_∞^1 norm defined over Ω_ξ^h as the maximum value among all the components of \cdot and among all the components of \cdot and its derivatives, respectively, evaluated at the domain quadrature points. In some of the convergence studies, the following non-dimensional angular frequency is also employed

$$\bar{\omega} = \frac{L_r^2}{\pi^2} \sqrt{\frac{\rho_r}{E_r \zeta^2}} \omega, \quad (34)$$

where L_r , ρ_r and E_r are suitably specified reference values of length, density and stiffness, respectively. Eventually, for transient analysis, time-integration is performed via a standard second-order accurate Newmark scheme [44].

4.1. Square plate

In the first set of tests, the square plate shown in Fig. 3(a), which schematically describes its geometry, boundary conditions and loads later considered in the transient analysis, is investigated. The geometry of the plate reference surface is described by the parametrization

$$\mathbf{x}_0 = \begin{pmatrix} \xi_1 \\ \xi_2 \\ 0 \end{pmatrix}, \quad \forall (\xi_1, \xi_2) \in [0, L] \times [0, L] \equiv \Omega_\xi. \quad (35)$$

where $L = 1$ m and $\zeta/L = 0.01$. The two different layups P₁ and P₂ in Table 2 are considered, for isotropic and laminated plate, respectively.

First the free-vibrations problem is considered. Fig. 4 shows the results of a hp -convergence analysis for the first eigenvalue and the associated eigenvector, for the proposed numerical scheme. In each diagram, the relevant error, either e_ω or e_U , is computed using the exact solution as the reference solution [37] and is plotted against $h/L = 1/n$, i.e. the ratio between the mesh element edge length h and the plate edge length L . Each curve corresponds to a different polynomial order p assumed in the DG scheme – Section 3 – as expressed through the label DG _{p} . The diagrams are grouped so that each row refers to a certain structural theory, namely FSDT, ED₁₁₁ and ED₃₃₃. On the other hand, each column refers to the results computed for an eigenvalue or the corresponding eigenvector, with either the layup P₁ or P₂. It is observed that the numerical scheme features convergence of order $\mathcal{O}(h^{p+1})$ for the eigenvector error and convergence of order $\mathcal{O}(h^{2(p-1)})$ for the eigenvalue error. It is worth noting that, although the results have

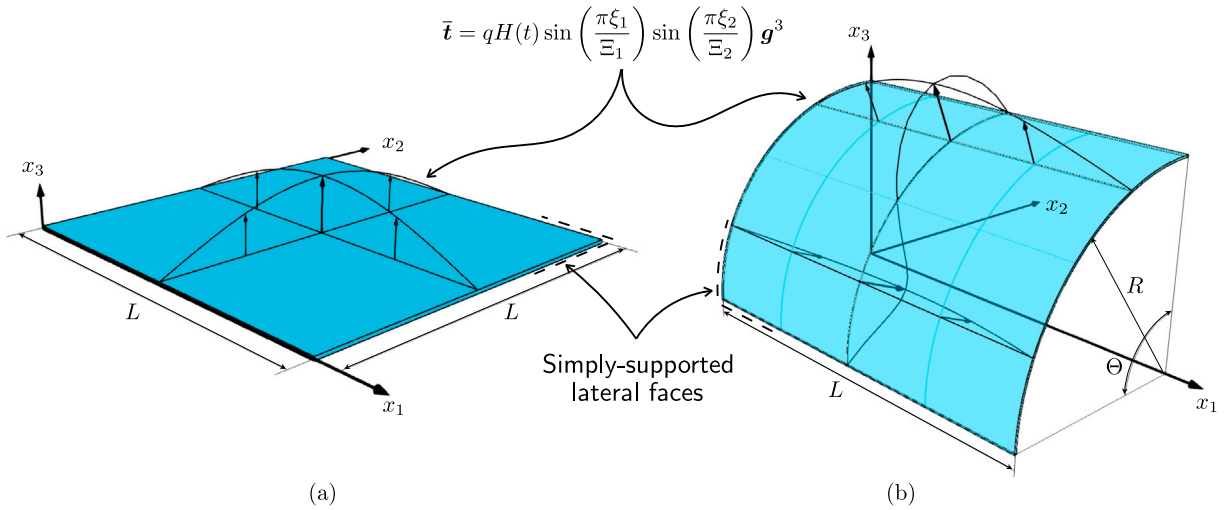


Fig. 3. Geometry, constraints and loads of the investigated (a) square plate and (b) cylindrical shell.

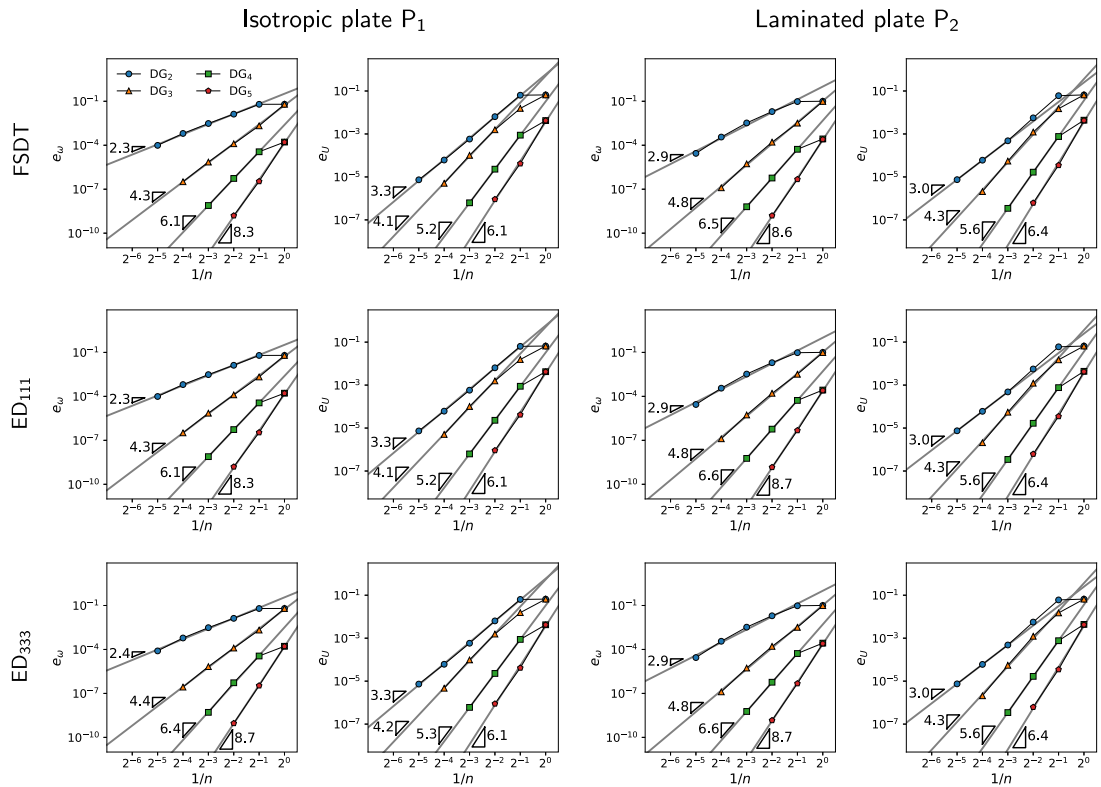


Fig. 4. hp -convergence analysis for the (first and third columns) first eigenvalue and the (second and fourth columns) first eigenvector for the free-vibration response of the analyzed square plate. Each row of diagrams groups results provided by the corresponding structural theory; the first two columns refer to the plate with layup P_1 , while the last two refer to the plate with layup P_2 .

been presented in terms of the first eigenvalue and associated eigenvector of the free-vibration problem, a convergence analysis for higher frequency modes is reported for the geometries considered in Sections 4.3 and 4.4.

A transient analysis is then performed for the laminated plate with layup P_2 , considering the dynamic loading term \bar{t} in Fig. 3(a), where q is assumed as unitary, being used in the non-dimensional measures of stress, $H(t)$ is the Heaviside step function, and $\Xi_1 = \Xi_2 = L$. The related results are reported in Fig. 5. In particular, Fig. 5(a,d) investigate the h -convergence of the plate dynamic

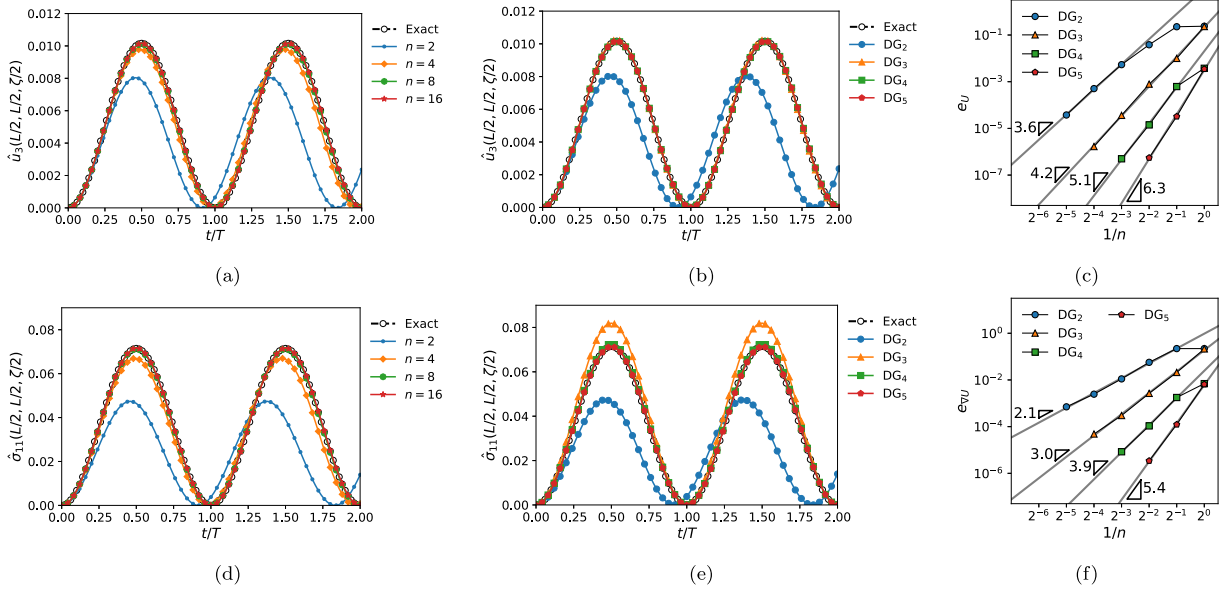


Fig. 5. Convergence assessment for the dynamic transient analysis of the laminated square plate with layup P_2 and constraints and loads specified in Fig. 3(a). The transient response is computed adopting the FSDT kinematic model. The h -convergence of the DG_2 scheme is investigated in terms of time history of (a) displacements and (d) stress components at the location $(\xi_1, \xi_2, \xi_3) = (L/2, L/2, \zeta/2)$. The p -convergence is investigated in terms of time histories of the same (b) displacement and (e) stress components, setting $n = 2$. The hp -convergence of the solution computed at $t = T/2$ is eventually investigated for the (c) displacement field and (f) its derivatives.

response, reporting the time history for the non-dimensional displacement and stress components

$$\hat{u}_3 \equiv \frac{\zeta^3}{L^4} u_3 \quad \text{and} \quad \hat{\sigma}_{11} \equiv \frac{\zeta^2}{L^2 q} \sigma_{11}, \tag{36}$$

sampled at the point $(\xi_1, \xi_2, \xi_3) = (L/2, L/2, \zeta/2)$, belonging to the plate’s top surface. The response of the plate for $t \in [0, 2T]$, with $T = 2\pi/\omega_1$, is reported as computed using the FSDT with DG_2 , i.e. polynomial interpolation degree $p = 2$ and $n = 2, 4, 8, 16$. The computed time histories are compared with the available exact solution and it is observed that the employed scheme provides satisfyingly accurate results when $n \geq 4$, both for the displacement and stress component. Fig. 5(b,e) show the time histories for the same non-dimensional components at the same physical location as computed selecting $n = 2$ and different orders of polynomial interpolation p for the DG_p scheme. The computed transient responses converge to the analytic exact solutions for both the displacement and stress components. Satisfying results are provided by $p \geq 3$ for the displacement and by $p \geq 4$ for the stress component. Eventually, Fig. 5(c) and (f) report the errors e_U and $e_{\nabla U}$ of the computed solutions with respect to the exact solutions at $t = T/2$, showing orders of convergence $\mathcal{O}(h^{p+1})$ and $\mathcal{O}(h^p)$, respectively.

4.2. Quarter of cylinder

The second application considers the cylindrical shell whose geometry, constraints and loads for the transient analysis are schematically depicted in Fig. 3(b). The shell geometry is described by the parametrization

$$\mathbf{x}_0 = \begin{pmatrix} \xi_2 \\ -R \sin(\xi_1) \\ R \cos(\xi_1) \end{pmatrix}, \quad \forall (\xi_1, \xi_2) \in [0, \Theta] \times [0, L] \equiv \Omega_\xi \tag{37}$$

where $R = 1$ m, $L/R = 2$, $\zeta/R = 0.01$, and $\Theta = \pi/2$.

First a free-vibrations analysis is performed, considering both sections C_1 and C_2 in Table 2, for isotropic and laminated shells respectively. Fig. 6 reports the results of a hp -convergence assessment of the first eigenvalues and the corresponding eigenvectors for the layups C_1 and C_2 . The results are presented and grouped analogously to what has been done for previous plate analysis. Also in this application the method features convergence of order $\mathcal{O}(h^{p+1})$ for the eigenvectors error and convergence of order $\mathcal{O}(h^{2(p-1)})$ for the eigenvalues error.

A transient dynamic analysis for the cylindrical shell with laminated layup C_2 is then performed. The shell is subject to the loads defined in Fig. 3(b) where, in the case of the cylindrical shell, $\Xi_1 = \Theta/2$ and $\Xi_2 = L$. The results are collected in Fig. 7 and presented analogously to what has been done for the above plate transient analysis. Fig. 7(a,d) investigate the h -convergence of the shell dynamic response, reporting the time history for the non-dimensional displacement and stress components

$$\hat{u}_{\xi_3} \equiv \frac{\zeta^2}{R^3} u_{\xi_3} \quad \text{and} \quad \hat{\sigma}_{11} \equiv \frac{\zeta}{Rq} \sigma_{11} \tag{38}$$

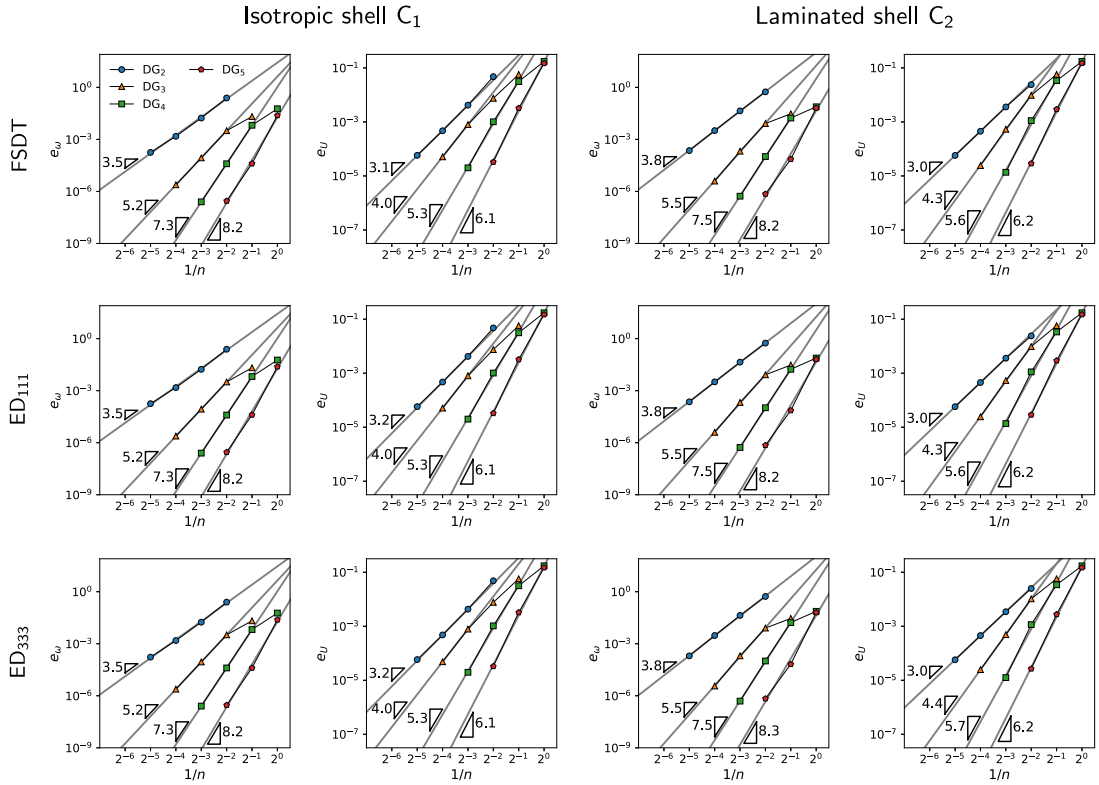


Fig. 6. hp -convergence analysis for the (first and third columns) first eigenvalue and the (second and fourth columns) first eigenvector for the free-vibration response of the analyzed cylindrical shell. Each row groups diagrams provided by the indicated structural theory – FSDT, ED₁₁₁, or ED₃₃₃; the first two columns refer to the plate with layup C₁, while the last two refer to the plate with layup C₂.

sampled at the point $(\xi_1, \xi_2, \xi_3) = (\Theta/4, L/2, \zeta/2)$. The shell transient response is computed for $t \in [0, 2T]$, with $T = 2\pi/\omega_1$, adopting a ED₃₃₃ structural theory coupled with a DG₂ scheme and $n = 2, 4, 8, 16$. It is observed that the computed transient responses converge to the available exact solutions, although more slowly than in the case of the plate, and satisfyingly accurate results are obtained only with the finer mesh, i.e. with $n = 16$. On the other hand, Fig. 5(b,e) show the time histories for the same non-dimensional components at the same physical location as computed selecting $n = 2$ and different polynomial orders p for the DG _{p} scheme. The computed responses converge to the analytic exact solutions for both the displacement and stress components and satisfying results are provided by $p \geq 3$ for both the displacement and stress component. Eventually, Fig. 7(c) and (f) show the errors e_U and $e_{\nabla U}$ of the numerical versus the exact solutions at $t = T/2$, revealing orders of convergence $\mathcal{O}(h^{p+1})$ and $\mathcal{O}(h^p)$, respectively, analogous to those observed in the plate analysis.

4.3. Circular plate

The circular plate shown in Fig. 8 is considered for the third set of tests. In this case, the reference surface Ω_ξ of the circular plate is defined using the implicit approach described in Section 3.3. In particular, upon employing the same mapping $\mathbf{x}_0 = \mathbf{x}_0(\xi_1, \xi_2)$ given in Eq. (35), where (ξ_1, ξ_2) span the background rectangle $R_\xi \equiv [0, 2R] \times [0, 2R]$, being $R = 1$ m, Ω_ξ is implicitly defined by the following level set function

$$\varphi = (\xi_1 - c_1)^2 + (\xi_2 - c_2)^2 - R^2, \tag{39}$$

where $c_1 = c_2 = R$. The considered circular plates have the isotropic and laminated sections denoted by P₁ and P₂ in Table 2, have thickness $\zeta/R = 0.01$ and are modeled using the FSDT. The discretization of the circular plate is obtained by dividing the background rectangle R_ξ using a $n \times n$ structured grid and following the procedure discussed in Section 3.3.

The results obtained for free-vibration problem are considered first. Table 3 shows the eigenvalues $\bar{\omega}_k$, with $k = 1, 2, 4, 6, 7$, for the isotropic circular plate, computed using a DG₄ scheme as a function of the mesh size $h = 2R/n$, with $n = 2, 3, 4, 6, 8$. With reference to Eq. (34), the non-dimensional eigenvalues are computed using $L_r = R$, $E_r = E$ and $\rho_r = \rho$, where E and ρ are the Young's modulus and the density, respectively, of the material M₁. In Table 3, the top row shows the implicitly defined mesh for each considered value of n , the second column from the right reports the converged FEM results, while the rightmost column shows the eigenmodes associated with each eigenvalue and computed by the present approach using the finest mesh.

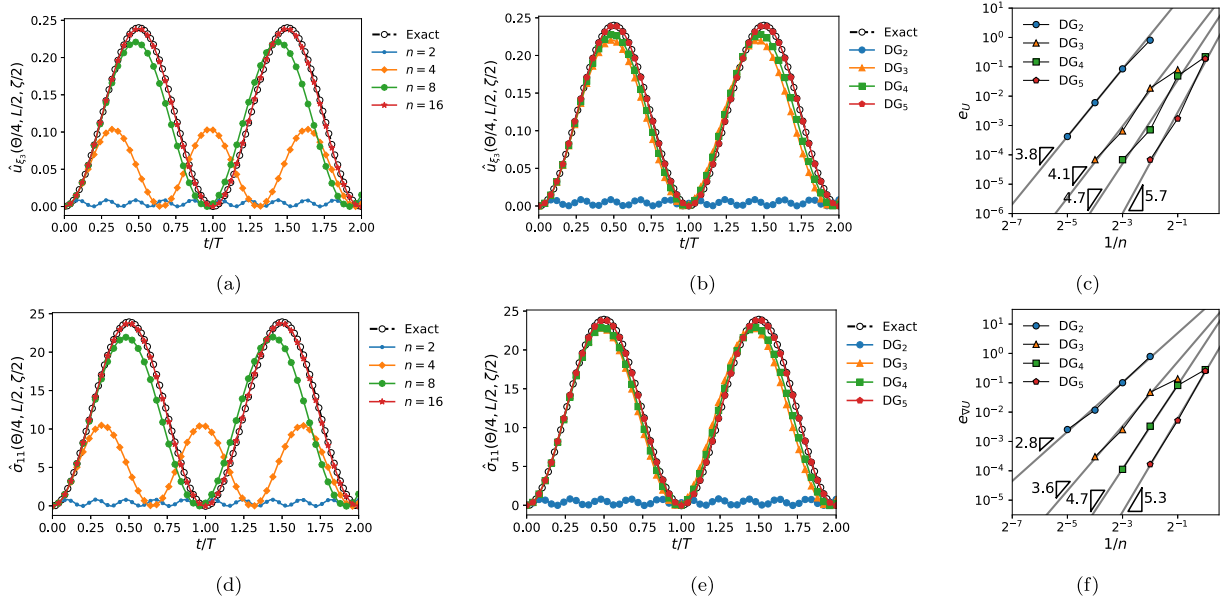


Fig. 7. Convergence assessment for the dynamic transient analysis of the laminated cylindrical shell with layup C_2 and constraints and loads specified in Fig. 3(b). The transient response is computed adopting the ED₃₃₃ kinematic model. The h -convergence of the DG₂ scheme is investigated in terms of time history of non-dimensional (a) displacements and (d) stress components at the location $(\xi_1, \xi_2, \xi_3) = (\Theta/4, L/2, \zeta/2)$. The p -convergence is investigated in terms of time histories of the same (b) displacement and (e) stress non-dimensional components, setting $n = 2$. The hp -convergence of the solution computed at $t = T/2$ is eventually investigated for the (c) displacement field and (f) its derivatives.

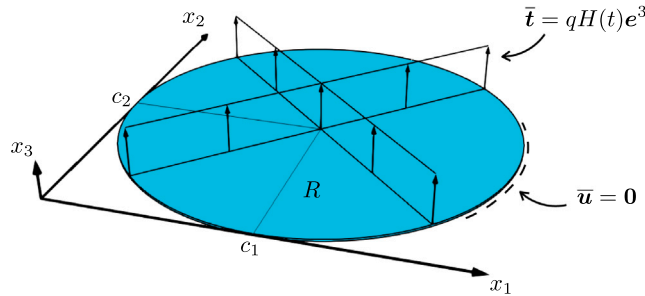


Fig. 8. Geometry, constraints and loads of the investigated circular plate.

Similarly, Table 4 shows some selected eigenvalues for the laminated circular plate computed using a DG₆ scheme and the same mesh sizes employed for the isotropic plate. In this case, the non-dimensional eigenvalues are computed using the Young’s modulus and the density of the material M_2 . The table also reports the converged FEM results and the eigenmodes associated with each eigenvalue.

In both the isotropic and the laminated plate cases, it is possible to observe that the proposed approach is able to recover the reference FEM solution; as expected, the higher the computed eigenvalue, the finer is the required mesh to achieve convergence. A more detailed convergence analysis is reported in Fig. 9, which illustrates a comparison between the present DG formulation and two FEM models in terms of computed eigenvalues versus the total number of degrees of freedom (DOF). In the plots of Fig. 9, each colored curve corresponds to the results obtained using a specific value p of the DG basis functions and different mesh sizes, while the dashed gray and black lines correspond to the results obtained via Abaqus’ S4R and S8R elements, respectively. Fig. 9(a,b) refer to the isotropic plate, while Fig. 9(c,d) refer to the laminated plate. In all cases, it is possible to observe the savings in terms of DOF enabled by the use of higher-order basis functions, which allows the proposed formulation to achieve faster convergence than FEM.

A transient analysis is then performed considering a uniform load \bar{t} applied over the top surface of the circular plate as sketched in Fig. 8. Similar to the square plate and cylindrical shell, the transient response is computed for $t \in [0, 2T]$, where $T = 2\pi/\omega_1$. The obtained results are reported in Fig. 10 for the isotropic plate case and in Fig. 11 for the laminated plate case. Fig. 10(a,c) and Fig. 11(a,c) illustrate the h -convergence of the transient response in terms of the following non-dimensional components of displacement and stress

$$\hat{u}_3 \equiv \frac{\zeta^2}{R^3} u_3 \quad \text{and} \quad \hat{\sigma}_{11} \equiv \frac{\zeta}{Rq} \sigma_{11}, \tag{40}$$

Table 3
Effect of the mesh size on some selected eigenvalues for the isotropic circular plate computed using the DG_4 scheme.




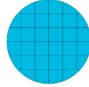
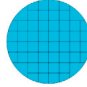
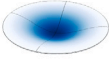
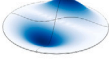
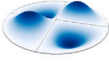
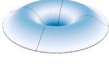

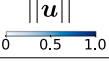
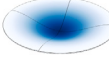
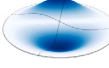
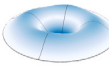
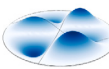
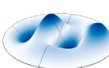
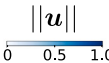
n	2	3	4	6	8	FEM	Eigenmode
Mesh							
$\bar{\omega}_1$	0.3091	0.3085	0.3086	0.3085	0.3085	0.3085	
$\bar{\omega}_2$	0.6560	0.6467	0.6426	0.6419	0.6419	0.6419	
$\bar{\omega}_4$	1.0819	1.0568	1.0580	1.0529	1.0527	1.0527	
$\bar{\omega}_6$	1.2291	1.2041	1.2056	1.2005	1.2004	1.2004	
$\bar{\omega}_7$	1.8944	1.6431	1.5777	1.5405	1.5399	1.5398	
							

Table 4
Effect of the mesh size on some selected eigenvalues for the laminated circular plate computed using the DG_6 scheme.

n	2	3	4	6	8	FEM	Eigenmode
$\bar{\omega}_1$	0.1738	0.1738	0.1738	0.1738	0.1738	0.1738	
$\bar{\omega}_2$	0.3602	0.3601	0.3602	0.3602	0.3602	0.3602	
$\bar{\omega}_6$	0.6675	0.6674	0.6674	0.6674	0.6674	0.6674	
$\bar{\omega}_7$	0.8348	0.8345	0.8346	0.8345	0.8345	0.8346	
$\bar{\omega}_{10}$	1.0409	1.0346	1.0346	1.0345	1.0345	1.0345	
							

computed using the DG_2 scheme. The p -convergence for the same displacement and stress components is reported in Fig. 10(b,d) and Fig. 11(b,d), for $n = 4$. The obtained results confirm the benefits of using high-order basis functions to obtain a converged solution, in terms of both displacement and stress components, using relatively coarse meshes.

4.4. Generally-curved shell

As the last set of tests, we consider the free-vibration response of the generally-curved shell shown in Fig. 12. The shell's reference surface is a B-spline surface [45] defined by the mapping

$$\mathbf{x}_0(\xi_1, \xi_2) = \sum_{k_1=0}^{K_1} \sum_{k_2=0}^{K_2} N_{k_1}^{q_1}(\xi_1) N_{k_2}^{q_2}(\xi_2) \mathbf{P}_{k_1, k_2}, \quad \forall (\xi_1, \xi_2) \in [0, 1] \times [0, 1] \equiv \Omega_\xi, \tag{41}$$

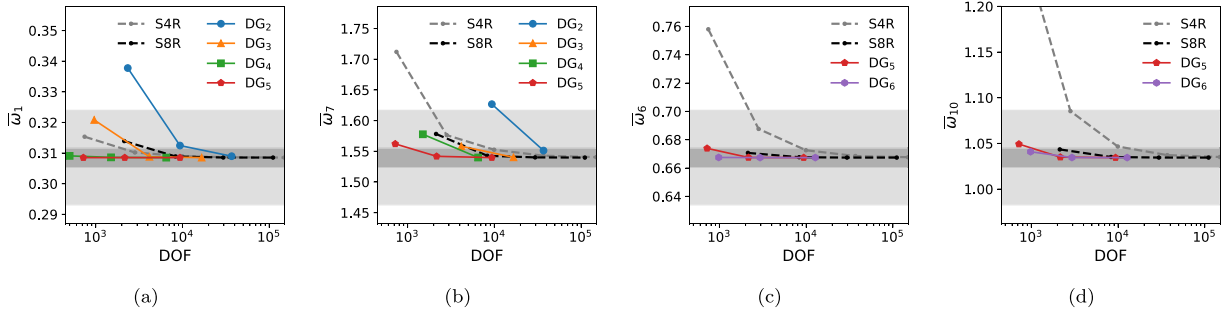


Fig. 9. Comparison between the proposed DG formulation and two FEM schemes in terms of computed eigenvalues vs number of degrees of freedom. Figures (a) and (b) refers to the first and seventh eigenvalues, respectively, for the isotropic circular plate, while figures (c) and (d) refers to the sixth and tenth eigenvalues, respectively, for the laminated circular plate. Light and dark gray areas denote the regions of less than 5% and 1% deviation, respectively, from the converged values. (For interpretation of the references to color in this figure legend, the reader is referred to the web version of this article.)

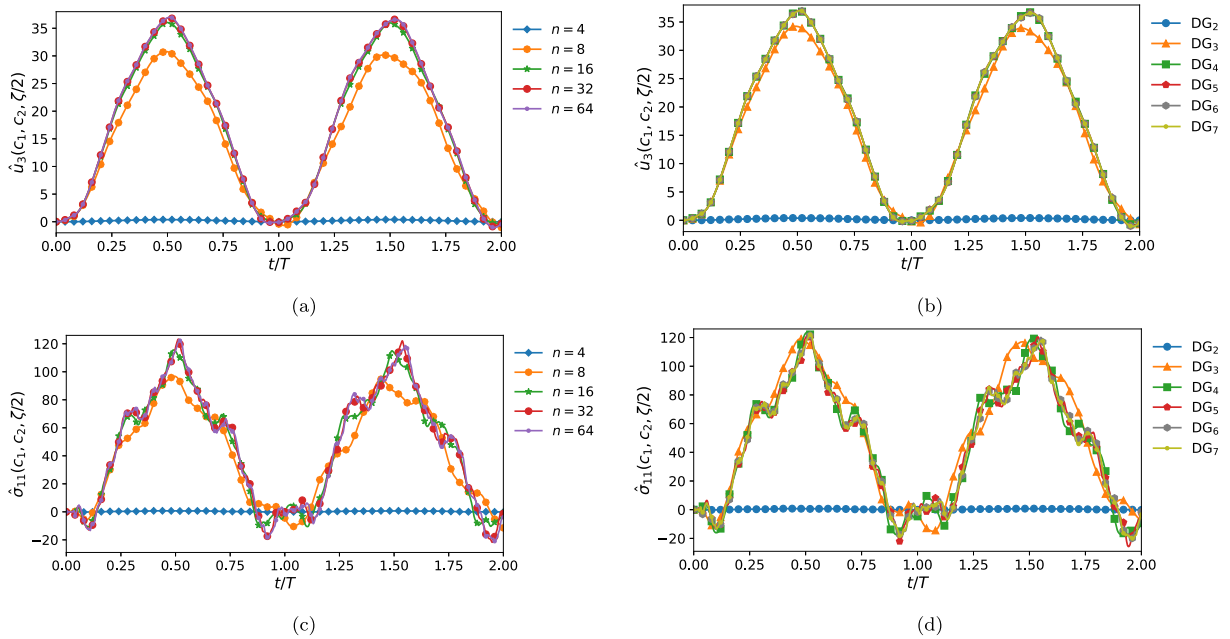


Fig. 10. Convergence assessment for the transient analysis of the isotropic circular plate having layup P_1 and modeled by the FSDT. The h -convergence of the DG_2 scheme is investigated in terms of time history of non-dimensional (a) displacements and (c) stress components at the location $(\xi_1, \xi_2, \xi_3) = (c_1, c_2, \zeta/2)$. The p -convergence is investigated for the same non-dimensional displacements and stress components in figures (b) and (d), respectively, setting $n = 4$.

where P_{k_1, k_2} , with $k_1 = 0, \dots, K_1$ and $k_2 = 0, \dots, K_2$, are the so-called control points, and $N_k^q(\xi)$ is the k th B-spline basis function of degree q . For the shell of Fig. 12, $K_1 = K_2 = 3$ and $q_1 = q_2 = 2$, while the control points are reported in Table 5.

The shell has thickness $\zeta = 0.01$ m, is made of the isotropic material M_1 reported in Table 1 and is modeled by the FSDT. A convergence analysis in terms of some selected computed eigenvalues as functions of DOF is reported in Fig. 13, which shows a comparison between the results obtained with the proposed formulation using different DG schemes and the results obtained using Abaqus' S4R and S8R elements. In this case, the non-dimensional eigenvalues are evaluated setting $E_r = E$ and $\rho_r = \rho$ of material M_1 and $L_r = 1$ m in Eq. (34). From Fig. 13, it is possible to notice that the present approach recovers the FEM results within an error of less than 3% and, similar to the case of the circular plate, higher-order basis functions enable faster convergence. Eventually, the computed eigenmodes associated with the eigenvalues of Fig. 13 are reported in Fig. 14 as contour plots of the magnitude of the displacement field. The figures also show the same contour levels of the eigenmodes computed using FEM as solid black lines, which match well with the contour levels computed using the present formulation, thus confirming its accuracy.

5. Discussion and further developments

In this study, a novel computational framework has been developed and assessed for the analysis of transient and free vibrations in composite laminated plates and shells. The proposed formulation allows the analysis of general laminated configurations as well

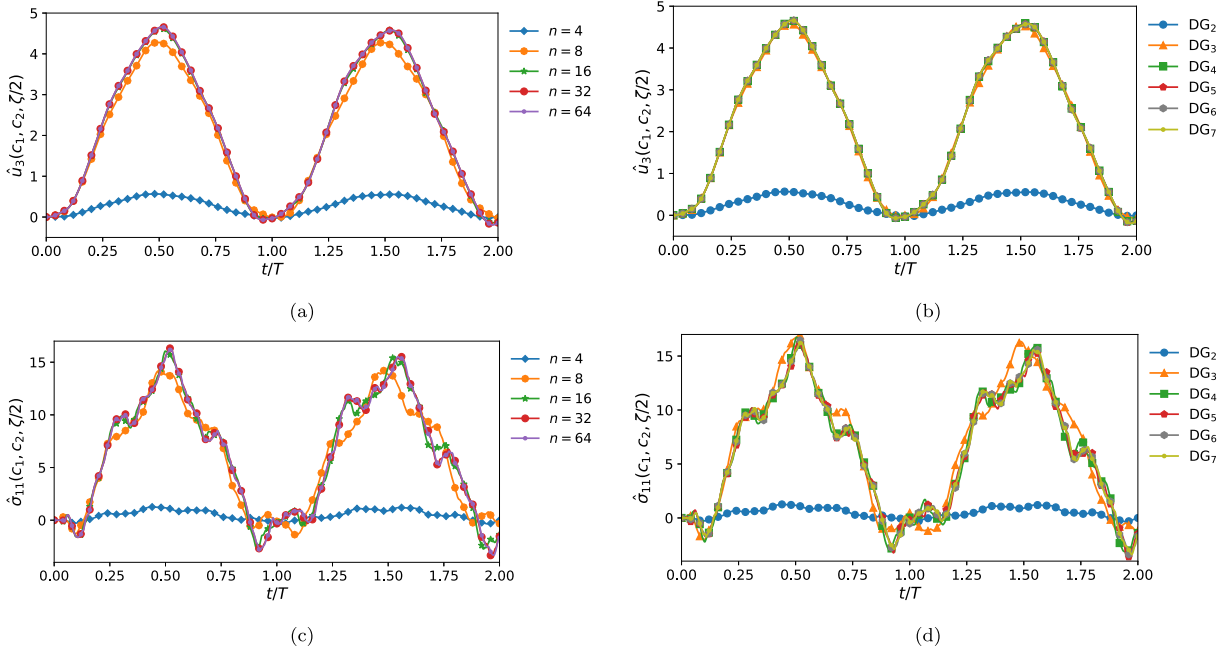


Fig. 11. Convergence assessment for the transient analysis of the laminated circular plate having layup P_2 and modeled by the FSDT. The h -convergence of the DG_2 scheme is investigated in terms of time history of non-dimensional displacements (a) displacements and (c) stress components at the location $(\xi_1, \xi_2, \xi_3) = (c_1, c_2, \zeta/2)$. The p -convergence is investigated for the same non-dimensional displacements and stress components in figures (b) and (d), respectively, setting $n = 4$.

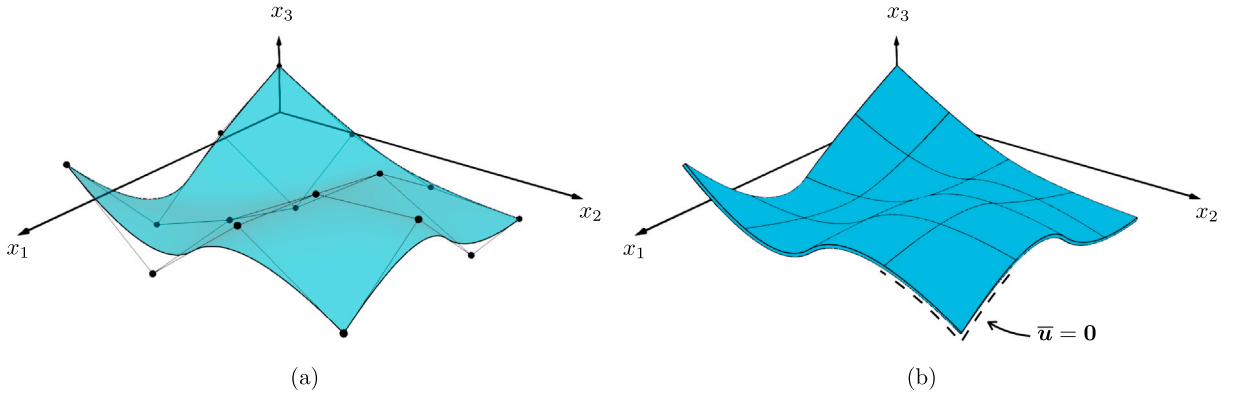


Fig. 12. (a) Control points and reference surface, and (b) geometry and boundary conditions of the investigated generally-curved shell.

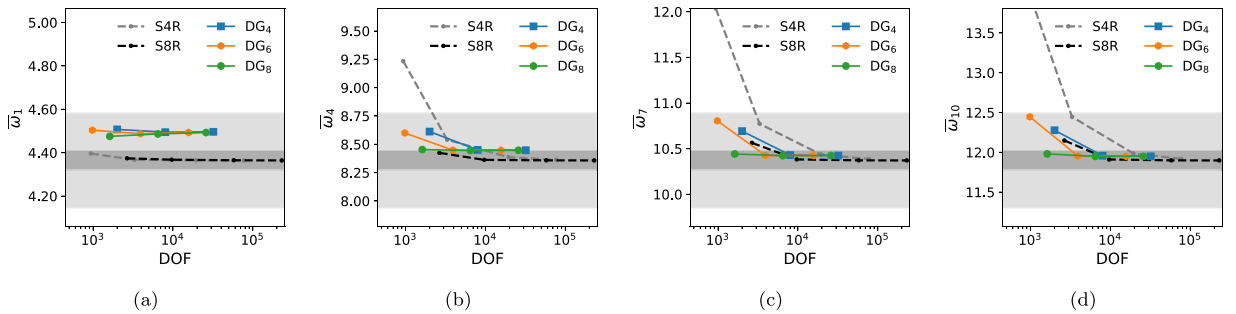


Fig. 13. Comparison between the proposed DG formulation and two FEM schemes in terms of computed eigenvalues vs number of degrees of freedom for the considered generally-curved shell. Light and dark gray areas denote the regions of less than 5% and 1% deviation, respectively, from the converged FEM values.

Table 5
Control points defining the reference surface of the generally-curved shell of Fig. 12.

P_{k_1, k_2} [m]	$k_1 = 0$	1	2	3
$k_2 = 0$	(0.0, 0.0, +0.1831)	(1/3, 0.0, +0.0263)	(2/3, 0.0, -0.1955)	(1.0, 0.0, +0.1495)
1	(0.0, 1/3, -0.0061)	(1/3, 1/3, -0.1650)	(2/3, 1/3, -0.0696)	(1.0, 1/3, -0.1007)
2	(0.0, 2/3, -0.1183)	(1/3, 2/3, +0.0601)	(2/3, 2/3, +0.1219)	(1.0, 2/3, +0.1659)
3	(0.0, 1.0, -0.1334)	(1/3, 1.0, -0.1146)	(2/3, 1.0, +0.1499)	(1.0, 1.0, -0.0208)

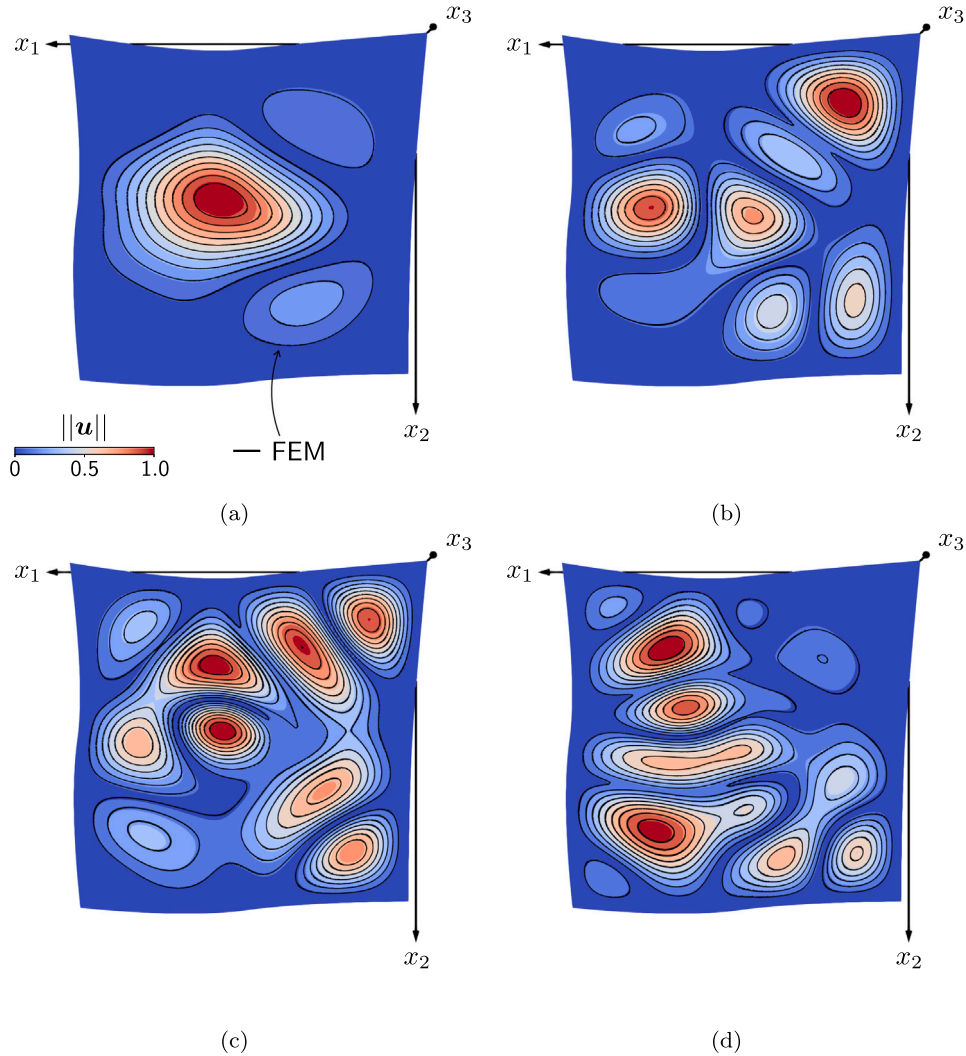


Fig. 14. Comparison between the results obtained by the proposed DG formulation (the contour plots) and those obtained by FEM (the solid lines) in terms of the computed eigenmodes for the generally-curved shell. Figures (a), (b), (c) and (d) refer to the first, fourth, seventh and tenth eigenmodes associated with the eigenvalues of the plots (a), (b), (c) and (d) of Fig. 13, respectively.

as general geometrical curvatures, thus providing an effective tool for the design of components with potential applications in the automotive and aerospace sectors. Owing to the combined use of variable-order ESL theories and DG methods, a key feature of the formulation is related to the possibility of tuning independently the order of the fields interpolations throughout both the shell thickness and the shell modeling domain, which allows tailoring the analysis to the application of interest. The high-order of accuracy of the formulation has been thoroughly assessed through several *hp*-convergence tests involving square and circular plates, cylindrical shells and generally-curved shells, ultimately demonstrating that a selected level of accuracy can be attained with a comparatively reduced number of degrees of freedom with respect to other numerical techniques, such as FEM.

The framework also offers several avenues for further research. First, the considered tests involve relatively simple geometries and material properties; therefore, a natural extension of the present study is the application of the proposed formulation to the

analysis of composite structures featuring multiple cutouts [46,47], through-the-thickness cracks [48,49], assembly of shells [28], and/or variable stiffness due to curved fiber placement [50,51]. Another interesting development could consist in moving beyond the assumptions of small strains and linear elastic constitutive behavior, so to investigate geometrical and material non-linearity and their effect on the free-vibration [52,53] and transient [54,55] response. Eventually, plate and shell problems involving multiple fields coupling, such as thermo-elasticity [56], piezo-electricity [57], or magneto-electro-elasticity [58,59], are of scientific and engineering interest in energy harvesting, morphing or structural health monitoring applications [60–62], and can benefit from the savings in terms of degrees of freedom offered by the present formulation to reduce the computational effort associated with the numerical analysis.

6. Conclusions

A novel high-order formulation for the dynamic analysis of general laminated shells has been developed and validated. Its key features can be summarized as follows: (i) the geometry of the shells can be described by a general mapping, thus allowing the modeling of structures with general curvature; (ii) a variable-order ESL approach based on the expansion of the covariant components of the displacement field allows tuning the order of approximation throughout the shell thickness; (iii) the use of the implicitly-defined mesh allows introducing curved boundaries in the space of the curvilinear coordinates while retaining the simplicity of generation of structured meshes; (iv) the developed DG methods allows using variable-order basis functions and solving the governing equations associated with a chosen ESL theory with high-order accuracy; (v) the obtained results show that the method offers high-order accuracy for the calculation of the eigenvectors, eigenfunctions and the transient response; (vi) the use of high-order basis functions enables faster convergence with respect to using standard finite elements, which has been measured in terms of error versus overall number of degrees of freedom.

CRedit authorship contribution statement

Vincenzo Gulizzi: Conceptualization, Data curation, Formal analysis, Investigation, Methodology, Software, Supervision, Validation, Visualization, Writing – original draft. **Ivano Benedetti:** Investigation, Methodology, Writing – original draft, Writing – review & editing, Formal analysis, Validation. **Alberto Milazzo:** Formal analysis, Investigation, Methodology, Validation, Writing – original draft, Writing – review & editing.

Declaration of competing interest

We have no known competing financial interests or personal relationships that could have appeared to influence the work reported in this paper.

Data availability

Data will be made available on request.

Acknowledgments

VG acknowledges the support by the European Union – Next Generation EU - PNRR M4 - C2 -investimento 1.1: Fondo per il Programma Nazionale di Ricerca e Progetti di Rilevante Interesse Nazionale (PRIN) - PRIN 2022 cod.2022AALLEC dal titolo “Hydrodynamic devices for micro-particle trapping and vibrational energy harvesting (HYDRA)” CUP B53D23005770006

IB and AM acknowledge the support by the European Union - Next Generation EU - National Sustainable Mobility Center CN00000023, Italian Ministry of University and Research - Decree n.1033 - 17/06/2022, Spokes 02/03, CUP B73C22000760001.

References

- [1] U.P. Breuer, *Commercial Aircraft Composite Technology*, vol. 115, Springer, 2016.
- [2] X. Zhang, Y. Chen, J. Hu, Recent advances in the development of aerospace materials, *Prog. Aerosp. Sci.* 97 (2018) 22–34, <http://dx.doi.org/10.1016/j.paerosci.2018.01.001>.
- [3] A. Muhammad, M.R. Rahman, R. Bains, M.K. Bin Bakri, 8 - Applications of sustainable polymer composites in automobile and aerospace industry, in: M.R. Rahman (Ed.), *Advances in Sustainable Polymer Composites*, in: Woodhead Publishing Series in Composites Science and Engineering, Woodhead Publishing, 2021, pp. 185–207, <http://dx.doi.org/10.1016/B978-0-12-820338-5.00008-4>.
- [4] A. Wazeer, A. Das, C. Abeykoon, A. Sinha, A. Karmakar, Composites for electric vehicles and automotive sector: A review, *Green Energy Intell. Transp.* 2 (1) (2023) 100043, <http://dx.doi.org/10.1016/j.geits.2022.100043>.
- [5] P. Parandoush, D. Lin, A review on additive manufacturing of polymer-fiber composites, *Compos. Struct.* 182 (2017) 36–53, <http://dx.doi.org/10.1016/j.compstruct.2017.08.088>.
- [6] K. Yassin, M. Hojjati, Processing of thermoplastic matrix composites through automated fiber placement and tape laying methods: A review, *J. Thermoplast. Compos. Mater.* 31 (12) (2018) 1676–1725, <http://dx.doi.org/10.1177/0892705717738305>.
- [7] J. Llorca, C. González, J.M. Molina-Aldareguía, J. Segurado, R. Seltzer, F. Sket, M. Rodríguez, S. Sádaba, R. Muñoz, L.P. Canal, Multiscale modeling of composite materials: a roadmap towards virtual testing, *Adv. Mater.* 23 (44) (2011) 5130–5147, <http://dx.doi.org/10.1002/adma.201101683>.
- [8] O. Falcó, R. Ávila, B. Tjjs, C. Lopes, Modelling and simulation methodology for unidirectional composite laminates in a Virtual Test Lab framework, *Compos. Struct.* 190 (2018) 137–159, <http://dx.doi.org/10.1016/j.compstruct.2018.02.016>.

- [9] A. Benaouali, S. Kachel, Multidisciplinary design optimization of aircraft wing using commercial software integration, *Aerosp. Sci. Technol.* 92 (2019) 766–776, <http://dx.doi.org/10.1016/j.ast.2019.06.040>.
- [10] M. Griffo, A. Da Ronch, I. Benedetti, A computational aeroelastic framework based on high-order structural models and high-fidelity aerodynamics, *Aerosp. Sci. Technol.* 132 (2023) 108069, <http://dx.doi.org/10.1016/j.ast.2022.108069>.
- [11] M. Griffo, V. Gulizzi, A. Milazzo, A. Da Ronch, I. Benedetti, High-fidelity aeroelastic transonic analysis using higher-order structural models, *Compos. Struct.* 321 (2023) 117315, <http://dx.doi.org/10.1016/j.compstruct.2023.117315>.
- [12] S. Boria, J. Obradovic, G. Belingardi, Experimental and numerical investigations of the impact behaviour of composite frontal crash structures, *Composites B* 79 (2015) 20–27, <http://dx.doi.org/10.1016/j.compositesb.2015.04.016>.
- [13] A. Tabiei, W. Zhang, Composite laminate delamination simulation and experiment: A review of recent development, *Appl. Mech. Rev.* 70 (3) (2018) 030801, <http://dx.doi.org/10.1115/1.4040448>.
- [14] D. Rajpal, F. Mitrotta, C. Socci, J. Sodja, C. Kassapoglou, R. De Breucker, Design and testing of aeroelastically tailored composite wing under fatigue and gust loading including effect of fatigue on aeroelastic performance, *Compos. Struct.* 275 (2021) 114373, <http://dx.doi.org/10.1016/j.compstruct.2021.114373>.
- [15] E. Carrera, M. Cinefra, M. Petrolo, E. Zappino, *Finite Element Analysis of Structures Through Unified Formulation*, John Wiley & Sons, 2014.
- [16] E. Carrera, E. Zappino, Carrera unified formulation for free-vibration analysis of aircraft structures, *AIAA J.* 54 (1) (2016) 280–292, <http://dx.doi.org/10.2514/1.J054265>.
- [17] A. Vigiotti, E. Zappino, E. Carrera, Free vibration analysis of variable angle-tow composite wing structures, *Aerosp. Sci. Technol.* 92 (2019) 114–125, <http://dx.doi.org/10.1016/j.ast.2019.05.068>.
- [18] A. De Miguel, A. Pagani, E. Carrera, Higher-order structural theories for transient analysis of multi-mode Lamb waves with applications to damage detection, *J. Sound Vib.* 457 (2019) 139–155, <http://dx.doi.org/10.1016/j.jsv.2019.05.053>.
- [19] M. Amabili, J. Reddy, The nonlinear, third-order thickness and shear deformation theory for statics and dynamics of laminated composite shells, *Compos. Struct.* 244 (2020) 112265, <http://dx.doi.org/10.1016/j.compstruct.2020.112265>.
- [20] K. Liew, J. Wang, T. Ng, M. Tan, Free vibration and buckling analyses of shear-deformable plates based on FSDT meshfree method, *J. Sound Vib.* 276 (3–5) (2004) 997–1017, <http://dx.doi.org/10.1016/j.jsv.2003.08.026>.
- [21] S. Hu, R. Zhong, Q. Wang, Q. Bin, Vibration analysis of closed laminate conical, cylindrical shells and annular plates using meshfree method, *Eng. Anal. Bound. Elem.* 133 (2021) 341–361, <http://dx.doi.org/10.1016/j.enganabound.2021.09.011>.
- [22] M.H.G. Rad, S.M. Hosseini, The modified CUF-EFG method for the dynamic analysis of GPLs-CNTs-reinforced FG multilayer thick cylindrical shells under shock loadings: A modified meshless implementation, *Eng. Anal. Bound. Elem.* 156 (2023) 499–518, <http://dx.doi.org/10.1016/j.enganabound.2023.08.023>.
- [23] Y. Kumar, The Rayleigh–Ritz method for linear dynamic, static and buckling behavior of beams, shells and plates: A literature review, *J. Vib. Control* 24 (7) (2018) 1205–1227, <http://dx.doi.org/10.1177/1077546317694724>.
- [24] L. Dozio, E. Carrera, A variable kinematic Ritz formulation for vibration study of quadrilateral plates with arbitrary thickness, *J. Sound Vib.* 330 (18–19) (2011) 4611–4632, <http://dx.doi.org/10.1016/j.jsv.2011.04.022>.
- [25] D. Zhou, S. Lo, F. Au, Y. Cheung, W. Liu, 3-D vibration analysis of skew thick plates using Chebyshev–Ritz method, *Int. J. Mech. Sci.* 48 (12) (2006) 1481–1493, <http://dx.doi.org/10.1016/j.ijmecsci.2006.06.015>.
- [26] A. Milazzo, Free vibrations analysis of cracked variable stiffness composite plates by the eXtended Ritz method, *Mech. Adv. Mater. Struct.* 30 (8) (2023) 1675–1691, <http://dx.doi.org/10.1080/15376494.2022.2038742>.
- [27] K.M. Liew, T.Y. Ng, X. Zhao, Free vibration analysis of conical shells via the element-free kp-Ritz method, *J. Sound Vib.* 281 (3–5) (2005) 627–645, <http://dx.doi.org/10.1016/j.jsv.2004.01.005>.
- [28] G. Sciascia, V. Oliveri, A. Milazzo, P.M. Weaver, Ritz solution for transient analysis of variable-stiffness shell structures, *AIAA J.* 58 (4) (2020) 1796–1810, <http://dx.doi.org/10.2514/1.J058686>.
- [29] V. Gulizzi, I. Benedetti, A. Milazzo, An implicit mesh discontinuous Galerkin formulation for higher-order plate theories, *Mech. Adv. Mater. Struct.* 27 (17) (2020) 1494–1508, <http://dx.doi.org/10.1080/15376494.2018.1516258>.
- [30] V. Gulizzi, I. Benedetti, A. Milazzo, A high-resolution layer-wise discontinuous Galerkin formulation for multilayered composite plates, *Compos. Struct.* 242 (2020) 112137, <http://dx.doi.org/10.1016/j.compstruct.2020.112137>.
- [31] G. Guarino, V. Gulizzi, A. Milazzo, High-fidelity analysis of multilayered shells with cut-outs via the discontinuous Galerkin method, *Compos. Struct.* 276 (2021) 114499, <http://dx.doi.org/10.1016/j.compstruct.2021.114499>.
- [32] J.S. Hesthaven, T. Warburton, High-order nodal discontinuous Galerkin methods for the Maxwell eigenvalue problem, *Philos. Trans. R. Soc. Lond. Ser. A Math. Phys. Eng. Sci.* 362 (1816) (2004) 493–524, <http://dx.doi.org/10.1098/rsta.2003.1332>.
- [33] P.F. Antonietti, A. Buffa, I. Perugia, Discontinuous Galerkin approximation of the Laplace eigenproblem, *Comput. Methods Appl. Mech. Engrg.* 195 (25–28) (2006) 3483–3503, <http://dx.doi.org/10.1016/j.cma.2005.06.023>.
- [34] G. Guarino, V. Gulizzi, A. Milazzo, Accurate multilayered shell buckling analysis via the implicit-mesh discontinuous Galerkin method, *AIAA J.* 60 (12) (2022) 6854–6868, <http://dx.doi.org/10.2514/1.J061933>.
- [35] G. Guarino, A. Milazzo, V. Gulizzi, Equivalent-Single-Layer discontinuous Galerkin methods for static analysis of multilayered shells, *Appl. Math. Model.* 98 (2021) 701–721, <http://dx.doi.org/10.1016/j.apm.2021.05.024>.
- [36] R.M. Jones, *Mechanics of Composite Materials*, CRC Press, 2018.
- [37] J.N. Reddy, *Mechanics of Laminated Composite Plates and Shells: Theory and Analysis*, CRC Press, 2003.
- [38] V. Gulizzi, I. Benedetti, A. Milazzo, High-order accurate beam models based on discontinuous Galerkin methods, *Aerotec. Missili Spaz.* (2023) 1–16, <http://dx.doi.org/10.1007/s42496-023-00168-3>.
- [39] I. Benedetti, V. Gulizzi, A. Milazzo, Layer-wise discontinuous Galerkin methods for piezoelectric laminates, *Modelling* 1 (2) (2020) 198–214, <http://dx.doi.org/10.3390/modelling1020012>.
- [40] R. Saye, Implicit mesh discontinuous Galerkin methods and interfacial gauge methods for high-order accurate interface dynamics, with applications to surface tension dynamics, rigid body fluid–structure interaction, and free surface flow: Part I, *J. Comput. Phys.* 344 (2017) 647–682, <http://dx.doi.org/10.1016/j.jcp.2017.04.076>.
- [41] R. Saye, Implicit mesh discontinuous Galerkin methods and interfacial gauge methods for high-order accurate interface dynamics, with applications to surface tension dynamics, rigid body fluid–structure interaction, and free surface flow: Part II, *J. Comput. Phys.* 344 (2017) 683–723, <http://dx.doi.org/10.1016/j.jcp.2017.05.003>.
- [42] V. Gulizzi, A.S. Almgren, J.B. Bell, A coupled discontinuous Galerkin-Finite Volume framework for solving gas dynamics over embedded geometries, *J. Comput. Phys.* 450 (2022) 110861, <http://dx.doi.org/10.1016/j.jcp.2021.110861>.
- [43] V. Gulizzi, R. Saye, Modeling wave propagation in elastic solids via high-order accurate implicit-mesh discontinuous Galerkin methods, *Comput. Methods Appl. Mech. Engrg.* 395 (2022) 114971, <http://dx.doi.org/10.1016/j.cma.2022.114971>.
- [44] K.-J. Bathe, *Finite Element Procedures*, Klaus-Jürgen Bathe, 2006.
- [45] L. Piegl, W. Tiller, *The NURBS Book*, Springer Science & Business Media, 1996.
- [46] X. Sun, P. Zhang, H. Qiao, K. Lin, High-order free vibration analysis of elastic plates with multiple cutouts, *Arch. Appl. Mech.* 91 (2021) 1837–1858, <http://dx.doi.org/10.1007/s00419-020-01857-2>.

- [47] Z. Jing, Variable stiffness discrete Ritz method for free vibration analysis of plates in arbitrary geometries, *J. Sound Vib.* 553 (2023) 117662, <http://dx.doi.org/10.1016/j.jsv.2023.117662>.
- [48] M. Bachene, R. Tiberkak, S. Rechak, Vibration analysis of cracked plates using the extended finite element method, *Arch. Appl. Mech.* 79 (2009) 249–262, <http://dx.doi.org/10.1007/s00419-008-0224-7>.
- [49] J. Xue, Y. Wang, Free vibration analysis of a flat stiffened plate with side crack through the Ritz method, *Arch. Appl. Mech.* 89 (2019) 2089–2102, <http://dx.doi.org/10.1007/s00419-019-01565-6>.
- [50] W. Zhao, R.K. Kapania, Prestressed vibration of stiffened variable-angle tow laminated plates, *AIAA J.* 57 (6) (2019) 2575–2593, <http://dx.doi.org/10.2514/1.J057719>.
- [51] G. Sciascia, V. Oliveri, P.M. Weaver, Dynamic analysis of prestressed variable stiffness composite shell structures, *Thin-Walled Struct.* 175 (2022) 109193, <http://dx.doi.org/10.1016/j.tws.2022.109193>.
- [52] I. Benedetti, V. Gulizzi, A. Milazzo, X-Ritz solution for nonlinear free vibrations of plates with embedded cracks, *Aerotec. Missili Spaz.* 98 (2019) 75–83, <http://dx.doi.org/10.1007/s42496-019-00006-5>.
- [53] F.A.X.C. Pinho, M. Amabili, Z.J.G.N. Del Prado, F.M.A.d. Silva, Nonlinear free vibration analysis of doubly curved shells, *Nonlinear Dynam.* 111 (23) (2023) 21535–21555, <http://dx.doi.org/10.1007/s11071-023-08963-0>.
- [54] I. Choi, Geometrically nonlinear transient analysis of composite laminated plate and shells subjected to low-velocity impact, *Compos. Struct.* 142 (2016) 7–14, <http://dx.doi.org/10.1016/j.compstruct.2016.01.070>.
- [55] A. Milazzo, I. Benedetti, A non-linear Ritz method for the analysis of low velocity impact induced dynamics in variable angle tow composite laminates, *Compos. Struct.* 276 (2021) 114533, <http://dx.doi.org/10.1016/j.compstruct.2021.114533>.
- [56] E. Carrera, S. Valvano, A variable ESL/LW kinematic plate formulation for free-vibration thermoelastic analysis of laminated structures, *J. Therm. Stresses* 42 (4) (2019) 452–474, <http://dx.doi.org/10.1080/01495739.2018.1474513>.
- [57] A. Milazzo, C. Orlando, An equivalent single-layer approach for free vibration analysis of smart laminated thick composite plates, *Smart Mater. Struct.* 21 (7) (2012) 075031, <http://dx.doi.org/10.1088/0964-1726/21/7/075031>.
- [58] A. Milazzo, I. Benedetti, C. Orlando, et al., Boundary element method for magneto electro elastic laminates, *Comput. Model. Eng. Sci.* 15 (1) (2006) 17.
- [59] K.K. Żur, M. Arefi, J. Kim, J.N. Reddy, Free vibration and buckling analyses of magneto-electro-elastic FGM nanoplates based on nonlocal modified higher-order sinusoidal shear deformation theory, *Composites B* 182 (2020) 107601, <http://dx.doi.org/10.1016/j.compositesb.2019.107601>.
- [60] S.A. Emam, D.J. Inman, A review on bistable composite laminates for morphing and energy harvesting, *Appl. Mech. Rev.* 67 (6) (2015) 060803, <http://dx.doi.org/10.1115/1.4032037>.
- [61] D. Tang, E. Dowell, Aeroelastic response and energy harvesting from a cantilevered piezoelectric laminated plate, *J. Fluids Struct.* 76 (2018) 14–36, <http://dx.doi.org/10.1016/j.jfluidstructs.2017.09.007>.
- [62] V. Giurgiutiu, G. Santoni-Bottai, Structural health monitoring of composite structures with piezoelectric-wafer active sensors, *AIAA J.* 49 (3) (2011) 565–581, <http://dx.doi.org/10.1080/01495739.2018.1474513>.